Robust Secure ISAC Beamforming for Integrated HAPS-LEO Maritime Networks

Nanchi Su, *Member, IEEE,* Zhongxiang Wei, *Senior Member, IEEE,* Xiaoye Jing, *Member, IEEE,* Yao Shi, *Member, IEEE,* Weijie Yuan, *Senior Member, IEEE,* Qinyu Zhang, *Senior Member, IEEE,* and Tse-Tin Chan, *Member, IEEE*

***Abstract*—Maritime integrated sensing and communication (ISAC) systems face dual challenges: achieving precise target estimation under heavy sea clutter while preventing eavesdropping in open wireless channels. This paper addresses secure beamforming design for high-altitude platform stations (HAPS) and low Earth orbit (LEO) satellites serving maritime regions. We formulate a joint optimization problem that balances sensing accuracy, measured by the Bayesian Cramér-Rao bound (BCRB) under spherically invariant random process (SIRP) clutter, against worst-case secrecy rate (SR) over an eavesdropper angular sector. We optimize this sensing-secrecy trade-off by jointly designing the beamforming vector, Bob-null artificial noise (AN) covariance, and pulse compression filter via an alternating optimization algorithm with provable convergence guarantees. For LEO scenarios, we extend the framework through per-slot parameterization that absorbs Doppler-induced inter-carrier interference (ICI) into effective noise terms, enabling warm-started optimization across orbital passes without altering the core algorithm. Simulations demonstrate smooth trade-offs among sensing and secrecy, robustness to sea state variations, and stable performance across LEO time slots under maritime conditions.**

***Index Terms*—Integrated sensing and communication, physical layer security, Bayesian Cramér-Rao bound, artificial noise, high-altitude platform stations, low Earth orbit satellites, maritime communications**

I. Introduction

This work was supported in part by National Natural Science Foundation of China under Grant 62027802, 62401181, 62201174, 62501153, 62531012; in part by the National Key Laboratory of Avionics Integration and Aviation System-of Systems Synthesis under Grant 2025AIASS0701; in part by the Fundamental Research Funds for the Central Universities; in part by Shanghai Municipal Science and Technology Program Projects under Grant 25ZR1401361; in part by Shenzhen Science and Technology Program under Grant KQTD20210811090116029; in part by Dongguan Strategic Scientist Teams Project under Grant 20241900700013; in part by the Research Matching Grant Scheme from the Research Grants Council of Hong Kong.

(Corresponding author: Tse-Tin Chan.)

N. Su, Y. Shi, and Q. Zhang are with Guangdong Provincial Key Laboratory of Aerospace Communication and Networking Technology, Harbin Institute of Technology (Shenzhen), Shenzhen 518055, China; N. Su is also with the Department of Mathematics and Information Technology, The Education University of Hong Kong, Hong Kong, China (e-mail: {sunanchi, shiyao, zqy}@hit.edu.cn).

Z. Wei is with the College of Electronic and Information Engineering, and Shanghai Institute of Intelligent Science and Technology, Tongji University, Shanghai 201804, China (e-mail: z_wei@tongji.edu.cn).

X. Jing is with School of Electrical Engineering & Intelligentization, Dongguan University of Technology, Dongguan 523808, China (e-mail: jingxiaoye@dgut.edu.cn).

W. Yuan is with the School of Automation and Intelligent Manufacturing, Southern University of Science and Technology, Shenzhen 518055, China (e-mail: yuanwj@sustech.edu.cn).

T.-T. Chan is with the Department of Mathematics and Information Technology, The Education University of Hong Kong, Hong Kong, China (e-mail: tsetinchan@eduhk.hk).

INTEGRATED sensing and communication (ISAC) has emerged as a cornerstone technology for sixth-generation (6G) wireless networks, enabling spectrum-efficient dual-functional systems that simultaneously provide communication services and radar sensing capabilities [1]. Maritime scenarios impose stringent requirements on wireless infrastructure: vessels, offshore platforms, and coastal facilities demand reliable connectivity over vast ocean areas where terrestrial base stations are infeasible [2]. High-altitude platform stations (HAPS) operating at stratospheric altitudes ($\sim$20 km) and low Earth orbit (LEO) satellites offer complementary solutions, providing persistent wide-area coverage while accommodating the harsh maritime propagation environment characterized by heavy sea clutter and extended line-of-sight (LoS) ranges.

The open nature of maritime wireless channels introduces critical security vulnerabilities. Unlike terrestrial networks where physical obstacles provide natural isolation, maritime communications are exposed to eavesdropping from vessels, aircraft, or adversarial platforms distributed across broad angular sectors. Traditional cryptographic methods assume secure key distribution, which becomes challenging in dynamic maritime environments with intermittent connectivity and heterogeneous user equipment. Physical layer security (PLS) techniques, particularly artificial noise (AN) injection and secure beamforming, offer complementary protection by exploiting spatial channel differences between legitimate users and eavesdroppers [3], degrading adversarial reception without requiring upper-layer key exchange.

Designing secure ISAC beamforming for maritime HAPS and LEO platforms faces the following fundamental challenges. First, maritime radar sensing must contend with heavy-tailed sea clutter whose amplitude statistics deviate significantly from Gaussian models [4], and the spherically invariant random process (SIRP) and K-distribution provide more accurate characterizations [5], but deriving tractable estimation bounds under non-Gaussian clutter remains nontrivial [6]–[8]. Second, eavesdropper channel state information (CSI) is typically unavailable or highly uncertain in maritime scenarios, necessitating robust security metrics that guarantee worst-case secrecy rate (SR) over angular sectors rather than relying on average or perfect-CSI assumptions [9], [10]. Third, LEO satellites move at 7$\sim$8 km/s, yielding Doppler shifts of several kHz (and often tens of kHz depending on carrier), which break orthogonal frequency-division multiplexing (OFDM) subcarrier orthogonality and cause ICI, while various Doppler/ICI compensation and orthogonal time frequency space (OTFS)-

type waveforms exist, a unified framework that keeps algorithmic consistency across HAPS and LEO ISAC remains lacking [11], [12]. Recent HAPS-enabled ISAC studies further underscore the need for such cross-platform designs [13]–[15].

Prior work on ISAC beamforming has predominantly focused on Gaussian noise environments with single-parameter estimation and either ignored security constraints or assumed perfect eavesdropper CSI [16]–[18]. Secure communication studies have explored AN-aided beamforming but rarely integrated radar sensing objectives or addressed maritime-specific clutter models. LEO satellite communications literature has tackled Doppler/ICI mitigation in isolation, without considering joint sensing-security trade-offs or algorithmic unification with HAPS platforms. Consequently, a rigorous framework that simultaneously addresses SIRP clutter modeling, worst-case sector secrecy, multi-parameter estimation bounds, and platform-agnostic LEO extensions remains absent.

This paper develops a secure ISAC beamforming framework for maritime networks integrating HAPS and LEO platforms. The core design jointly optimizes transmit beamforming, artificial noise injection, and radar signal processing to balance sensing accuracy and communication security. We stress that the framework is platform-agnostic and can be implemented on HAPS or LEO platforms separately using the same algorithmic structure, without requiring any HAPS–LEO cooperation. Sensing performance is quantified via the Bayesian Cramér-Rao bound under realistic SIRP sea clutter, capturing multi-parameter estimation accuracy (delay, angle, Doppler). Security is measured by worst-case secrecy rate over eavesdropper angular sectors, providing robust guarantees without requiring precise adversarial channel knowledge. An alternating optimization algorithm with provable convergence solves the resulting nonconvex problem through sequential convex approximations. For LEO scenarios, a per-slot parameterization framework absorbs Doppler-induced inter-carrier interference into effective noise terms, enabling consistent optimization across orbital passes without algorithmic modifications.

Within this scope, the contributions of our work are summarized as follows:

- We derive the BFIM under CES distributions for multi-parameter estimation (delay, angle, Doppler) under SIRP/K-distributed sea clutter, extending the Slepian–Bangs formula to non-Gaussian maritime environments.
- We formulate worst-case SR over eavesdropper angular sectors with Bob-null AN structure, eliminating the need for precise adversarial CSI while providing robust security guarantees.
- We jointly optimize the transmit beamformer, AN covariance, and pulse compression filter through an AO algorithm with provable convergence to stationary points and Lipschitz stability bounds justifying warm-start initialization.
- We extend the framework to LEO scenarios via per-slot parameterization that models Doppler-induced ICI as effective noise and performs worst-case optimization over discrete Doppler grids, maintaining algorithmic consistency across HAPS and LEO platforms.
- Simulations demonstrate smooth Pareto-optimal trade-offs, robustness to sea state variations, and stable convergence across LEO orbital passes.

The framework advances maritime ISAC by unifying rigorous clutter modeling, robust PLS, and platform-agnostic design, providing a foundation for secure dual-functional non-terrestrial networks (NTN) in 6G systems.

The remainder of the paper is organized as follows. Section II reviews related work on ISAC beamforming, PLS, and LEO satellite communications, highlighting key distinctions from prior studies. Section III presents the maritime ISAC signal model, including transmit signal structure, communication links, radar echo model with SIRP sea clutter, and pulse compression processing. Section IV derives the performance metrics: BFIM under CES distributions for sensing, and worst-case SR over eavesdropper angular sectors for security. Section V formulates the joint optimization problem and establishes its structural properties. Section VI-B develops the AO algorithm with convergence analysis. Section VII extends the framework to LEO scenarios via ICI-aware effective noise modeling and warm-start initialization. Section VIII presents numerical results demonstrating trade-off curves, sensitivity analysis, and LEO performance. Section IX concludes the paper and discusses future directions.

Notations: Unless otherwise specified, boldface lowercase letters $\mathbf{v}$ denote column vectors, and boldface uppercase letters $\mathbf{M}$ denote matrices. $\mathbb{C}^{m\times n}$ denotes the space of $m \times n$ complex matrices. $(\cdot)^T$, $(\cdot)^H$, and $(\cdot)^*$ denote transpose, conjugate transpose, and complex conjugate, respectively. $\|\mathbf{v}\|$ denotes the Euclidean norm of vector $\mathbf{v}$. $\mathrm{Tr}(\mathbf{M})$ denotes the trace of matrix $\mathbf{M}$. $\mathbf{I}_n$ denotes the $n \times n$ identity matrix. $\mathrm{diag}(\mathbf{v})$ denotes a diagonal matrix with vector $\mathbf{v}$ on the diagonal. $\otimes$ denotes the Kronecker product. $\mathrm{vec}(\mathbf{M})$ stacks the columns of matrix $\mathbf{M}$ into a column vector. $\mathbb{E}[\cdot]$ denotes statistical expectation. $\mathcal{CN}(\boldsymbol{\mu}, \mathbf{R})$ denotes a circularly symmetric complex Gaussian distribution with mean $\boldsymbol{\mu}$ and covariance $\mathbf{R}$. $\Re\{\cdot\}$ and $\Im\{\cdot\}$ denote the real and imaginary parts, respectively.

II. Related Work and Comparison

A. ISAC Beamforming

Integrated sensing and communication has emerged as a key technology for 6G wireless networks [1]. Recent works have explored beamforming design for ISAC systems with various performance metrics [19]–[21]. Liu *et al.* [1] provided a comprehensive overview of ISAC architectures and identified dual-functional beamforming as a central challenge. For joint radar-communication systems, the Cramér-Rao bound (CRB) has been widely adopted to quantify sensing performance [19], [22], [23]. However, most existing works focus on Gaussian noise models and single-parameter estimation (e.g., angle-of-arrival only), which may not adequately capture the complexity of maritime scenarios with heavy-tailed sea clutter and multi-parameter target states (delay, angle, Doppler) [17].

Our work extends the state of the art by adopting the BFIM under SIRP clutter [5], [24], enabling rigorous multi-parameter estimation bounds for realistic maritime environments. The log-det criterion provides a D-optimal design that balances estimation accuracy across all target parameters [25]–[27].

B. Physical Layer Security

Physical Layer Security (PLS) techniques have been extensively studied to protect wireless communications against eavesdropping without relying on cryptographic keys. AN injection and secure beamforming are two primary approaches. Mukherjee *et al.* [3] surveyed PLS principles in multiuser networks, highlighting the importance of worst-case SR metrics when eavesdropper CSI is imperfect [28]–[30].

Most prior works on secure ISAC assume either perfect eavesdropper CSI or average secrecy metrics, which may be overly optimistic for maritime scenarios where eavesdroppers can be located anywhere within a broad angular sector [23], [31]. Our approach adopts a worst-case SR over an eavesdropper angular sector, providing robust security guarantees. Furthermore, we structure the AN covariance to lie in Bob's null space, ensuring zero interference to the legitimate user while maximally degrading the eavesdropper's reception.

C. Maritime and Non-Terrestrial Networks

HAPS and LEO satellites offer promising solutions for maritime communications by providing wide-area coverage over ocean regions [32]–[34]. However, LEO satellites introduce significant Doppler shifts (up to ± 15 kHz at typical frequencies) due to orbital velocities of approximately 7.5 km/s, causing ICI in OFDM-based systems [35]–[37]. Existing works on LEO communications often address Doppler/ICI through heuristic compensation or simplified models [38], [39].

Our framework handles LEO-specific challenges through per-slot parameterization that absorbs Doppler-induced ICI into effective noise terms, enabling the core AO algorithm to remain unchanged across HAPS and LEO scenarios. This approach provides a unified design methodology while maintaining robustness to platform-specific dynamics.

D. Sea Clutter Modeling

Maritime radar systems must contend with sea clutter, which exhibits heavy-tailed amplitude distributions that deviate significantly from Gaussian models [6], [40]. The K-distribution and SIRP models have been widely adopted for sea clutter characterization [41]. Conte *et al.* [5] demonstrated that SIRP-based detectors achieve near-optimal performance in compound-Gaussian clutter. However, the impact of non-Gaussian clutter on Fisher information and parameter estimation bounds has received limited attention in the ISAC literature [42]. We incorporate SIRP/K-distributed sea clutter into the BCRB derivation using the generalized FIM for CES distributions [24], ensuring theoretical rigour while maintaining computational tractability.

The above studies have laid important foundations for ISAC beamforming, physical-layer security, maritime communications, and LEO Doppler compensation, but these topics are often treated separately. Most ISAC beamforming designs rely on Gaussian disturbance models and CRB-based sensing metrics in terrestrial or quasi-static scenarios [1], [17]–[20], while maritime sensing is strongly affected by heavy-tailed sea clutter. Secure ISAC and secure beamforming studies have explored artificial-noise-aided transmission and sensing-assisted eavesdropper estimation [23], [28]–[31], but they often require perfect/instantaneous Eve CSI or prior Eve localization. In contrast, this work adopts sector-based worst-case secrecy, and jointly optimizes transmit beamforming, Bob-null artificial noise, and pulse compression for delay-angle-Doppler sensing under SIRP/K-distributed clutter.

From the NTN perspective, existing maritime communication and satellite/LEO studies mainly focus on coverage, link-budget analysis, Doppler estimation, pre-compensation, OFDM/OTFS robustness, or link-level performance [2], [11], [12], [32]–[35], [37]–[39]. Different from these works, we embed Doppler-induced ICI into a unified secure ISAC beamforming framework rather than treating it only as a communication impairment. The proposed design therefore jointly accounts for non-Gaussian maritime clutter, uncertain Eve location, pulse-compression-aware sensing, and slot-wise LEO Doppler/ICI robustness, while using the same AO structure for both HAPS and LEO platforms.

III. Signal Model

We consider a maritime ISAC system anchored by a HAPS platform operating at stratospheric altitude, providing simultaneous communication and sensing services over wide ocean regions. The system serves a legitimate user (Bob) while sensing a potential eavesdropper (Eve) within an angular sector, and conducts radar surveillance of maritime targets. The signal model presented below applies to both HAPS and LEO platforms. Platform-specific effects (e.g., LEO Doppler variations) are incorporated through per-slot parameter updates while maintaining a unified baseband formulation. Section VII details the LEO extension.

While we first illustrate the system with HAPS, the AO algorithm is directly applicable to LEO platforms through per-slot parameterization (Sec. VII), maintaining algorithmic consistency across platforms without assuming cooperative transmission.

A. System Geometry

Consider a HAPS platform operating at stratospheric altitude, cruising at constant speed and quasi-stationary relative to the ground. It is notable that the HAPS platform typically provides a coverage radius of about 200–250 km over the maritime region at an altitude of approximately 20 km, providing a practical sense of the geographic scale considered. The platform is equipped with a uniform linear array (ULA) of N_t elements with element spacing $d = \lambda/2$, where λ is the wavelength corresponding to the carrier frequency f_c. The system bandwidth is denoted by B.

The time indexing includes slow-time pulse index $\ell = 0,\dots,L-1$ with pulse repetition interval T_r, and fast-time sampling index $n = 0,\dots,N-1$ with sampling interval $T_s = 1/B$. In the angle definition, θ represents the incident angle relative to the array normal. The target radial velocity v_r corresponds to Doppler shift $f_D = \frac{2v_r}{\lambda}$ (monostatic). Sea clutter has a near-zero mean Doppler with a spectral width determined by sea conditions.

The ULA steering vector is defined as:

$$\mathbf{a}_t(\theta) = \frac{1}{\sqrt{N_t}} \begin{bmatrix} 1 & e^{j2\pi\frac{d}{\lambda}\sin\theta} & \dots & e^{j2\pi\frac{d}{\lambda}(N_t-1)\sin\theta} \end{bmatrix}^T. \quad (1)$$

The single-pulse fast-time waveform $s[n]$ satisfies $\sum_n |s[n]|^2 = 1$. The transmit vector for the ℓ-th pulse is:

$$\mathbf{x}_\ell[n] = \mathbf{w}s[n] + \mathbf{v}_\ell[n], \quad \mathbf{v}_\ell[n] \sim \mathcal{CN}(\mathbf{0},\mathbf{Q}), \quad (2)$$

where $\mathbf{w} \in \mathbb{C}^{N_t}$ is the beamforming vector, $\mathbf{Q} \succeq \mathbf{0}$ is the AN covariance matrix, and the normalized transmit power constraint is $P_0 = \|\mathbf{w}\|_2^2 + \mathrm{tr}(\mathbf{Q}) \leq 1$.

B. Communication Links

The multiple-input single-output (MISO) channels for legitimate user Bob and potential eavesdropper Eve are denoted as $\mathbf{h}_b, \mathbf{h}_e \in \mathbb{C}^{N_t}$, respectively. We assume line-of-sight (LoS)-dominant (Rician) channels[1] and adopt the approximation $\mathbf{h}_b \approx \sqrt{\beta_b}\mathbf{a}_t(\theta_b)$ and $\mathbf{h}_e \approx \sqrt{\beta_e}\mathbf{a}_t(\theta_e)$, where β_b, β_e include large-scale pathloss and the non-line-of-sight (NLoS) components are neglected.

For the eavesdropper located within angular sector Θ_e [2], we model the channel as $\mathbf{h}_e(\theta) \approx \sqrt{\beta_e}\mathbf{a}_t(\theta)$ for $\theta \in \Theta_e$. In practice, Θ_e is discretized with angular grid spacing for computational tractability.

For the ℓ-th pulse in slow time:

$$\begin{aligned} y_{b,\ell}[n] &= e^{j2\pi\delta f_b \ell T_r}\mathbf{h}_b^H \mathbf{x}_\ell[n] + z_{b,\ell}[n], \\ y_{e,\ell}[n] &= e^{j2\pi\delta f_e \ell T_r}\mathbf{h}_e^H \mathbf{x}_\ell[n] + z_{e,\ell}[n], \end{aligned} \quad (3)$$

where $z_{b,\ell}[n] \sim \mathcal{CN}(0,\sigma_b^2)$ and $z_{e,\ell}[n] \sim \mathcal{CN}(0,\sigma_e^2)$ are additive white Gaussian noise, and $\delta f_b, \delta f_e$ represent residual carrier frequency offset (CFO) and Doppler shift after precompensation, such that $|\delta f_b|, |\delta f_e| \ll 1/T_r$ under HAPS. We keep the phase terms for generality.

C. Radar Echo at HAPS

The received signal vectors are $\mathbf{y}_\ell[n] \in \mathbb{C}^{N_r}$ for each fast-time sample n and slow-time pulse ℓ.

1) Target Return: Consider a target with azimuth θ_t, round-trip delay τ_t, and complex amplitude α_t. The HAPS uses a collocated transmit-receive array with $N_r = N_t$ elements. The baseband echo for the ℓ-th pulse at fast-time sample n is:

$$\mathbf{y}_\ell^{(\mathrm{tgt})}[n] = \alpha_t e^{j2\pi f_D \ell T_r}\mathbf{a}_r(\theta_t)\mathbf{a}_t^H(\theta_t)\mathbf{x}_\ell[n-\tau_t]. \quad (4)$$

Here, $\mathbf{a}_r(\cdot)$ is the receive array response (for collocated arrays, $\mathbf{a}_r = \mathbf{a}_t$), $\mathbf{x}_\ell[n-\tau_t]$ assumes delay aligns with the sampling grid, and α_t includes two-way pathloss and equivalent scattering/radar cross-section (RCS) terms [43]. The baseband model has absorbed the carrier frequency phase $e^{-j2\pi f_c \tau_t}$, and fractional delay is handled by interpolation in implementation[3].

[1]This assumption is well-justified for maritime HAPS/LEO scenarios due to the high altitude of the platforms and the open sea environment, which results in limited multipath components.

[2]The eavesdropper angular sector Θ_e accounts for possible motion of an adversarial vessel. For a vessel moving at speed v_e and located at distance R from the HAPS/LEO platform, the expected angular displacement over the update interval Δt is approximately $\Delta\theta \approx v_e\Delta t/R$. The sector width used in our simulations corresponds to this physical tracking uncertainty, providing a practical interpretation for the worst-case secrecy optimization.

[3]Fractional delays are implemented via interpolation, and we quantify their impact on BCRB in the sensitivity analysis of Sec. VIII.

2) Sea Clutter: We model the sea clutter as a spherically invariant random process (SIRP)[4]. For each pulse ℓ, the array snapshot is

$$\mathbf{c}_\ell[n] = \sqrt{\tau_\ell}\,\boldsymbol{\Sigma}_{c,\mathrm{ang}}^{1/2}\mathbf{u}_\ell[n], \quad (5)$$

where $\mathbf{u}_\ell[n] \sim \mathcal{CN}(\mathbf{0},\mathbf{I}_{N_r})$ is the speckle component, τ_ℓ is the texture (power modulation), and $\boldsymbol{\Sigma}_{c,\mathrm{ang}} \in \mathbb{C}^{N_r\times N_r}$ captures the spatial correlation [44]. Stacking L pulses yields the slow-time/space vector $\tilde{\mathbf{c}}$ whose covariance structure is

$$\boldsymbol{\Sigma}_{c,\mathrm{full}} = \boldsymbol{\Sigma}_{c,\mathrm{ang}} \otimes \boldsymbol{\Sigma}_{\mathrm{dop}} \in \mathbb{C}^{(N_rL)\times(N_rL)}, \quad (6)$$

where $\boldsymbol{\Sigma}_{\mathrm{dop}}$ is the Doppler correlation matrix generated by a Gaussian-type Doppler spectrum [45]:

$$r_c[\Delta\ell] = \exp\left(-2\pi^2\sigma_f^2(\Delta\ell T_r)^2\right), \quad (7)$$

with $\sigma_f \in \{2\,\mathrm{Hz}, 4\,\mathrm{Hz}, 6\,\mathrm{Hz}\}$ set according to sea state levels 2–4, and $\boldsymbol{\Sigma}_{c,\mathrm{ang}}$ follows a sinc/ULA angular correlation model.

The Kronecker-product form $\boldsymbol{\Sigma}_{c,\mathrm{full}} = \boldsymbol{\Sigma}_{c,\mathrm{ang}} \otimes \boldsymbol{\Sigma}_{\mathrm{dop}}$ is a separable approximation that enables tractable computation of the post-compression covariance and the BFIM. While exact separability may be slightly violated at high-grazing angles typical of LEO platforms, this approach captures the dominant angular and Doppler correlations and is commonly adopted in radar and maritime clutter modeling for computational tractability [5], [45].

The texture τ_ℓ follows an inverse-gamma distribution $\tau_\ell \sim \mathrm{Inv\text{-}Gamma}(\nu,\beta)$ with shape parameter $\nu = 2.0$ and scale parameter $\beta = 1$, producing a K-distributed clutter model. This choice ensures the texture mean $\mathbb{E}[\tau_\ell] = \beta/(\nu-1) = 1$ exists and is finite. In the post-compression radar output, the noise-plus-clutter covariance is denoted by $\mathbf{R}_{\mathrm{pc}}$ and is induced by $\boldsymbol{\Sigma}_{c,\mathrm{full}}$ (dimension made explicit where used).

The residual self-interference (SI) and thermal noise components are modeled as:

$$\mathbf{y}_\ell^{(\mathrm{SI})}[n] \sim \mathcal{CN}\big(\mathbf{0}, \sigma_{\mathrm{SI}}^2\boldsymbol{I}_{N_r}\big), \quad \mathbf{n}_\ell[n] \sim \mathcal{CN}\big(\mathbf{0}, \sigma_0^2\boldsymbol{I}_{N_r}\big). \quad (8)$$

After pulse compression, the effective covariance $\mathbf{R}_{\mathrm{pc}}$ induced by $\boldsymbol{\Sigma}_c$ and $\mathbf{h}_{\mathrm{pc}}$ is used in the post-compression statistics (see (10)).

3) Aggregate Radar Receive and Pulse Compression: The received signal at the array (before pulse compression) is:

$$\mathbf{y}_\ell[n] = \mathbf{y}_\ell^{(\mathrm{tgt})}[n] + \mathbf{c}_\ell[n] + \mathbf{y}_\ell^{(\mathrm{SI})}[n] + \mathbf{n}_\ell[n]. \quad (9)$$

Let $\mathbf{h}_{\mathrm{pc}} \in \mathbb{C}^{N\times 1}$ denote the pulse compression filter and $\mathbf{s} \in \mathbb{C}^{N\times 1}$ the fast-time signature of the target range cell. For pulse ℓ, we form the 2D observation matrix $\mathbf{Y}_\ell \in \mathbb{C}^{N_r\times N}$ with $[\mathbf{Y}_\ell]_{i,n} = [\mathbf{y}_\ell[n]]_i$ (spatial element i, fast-time sample n).

[4]SIRP choice and impact on FIM: The SIRP/K-distributed clutter model falls within the broader class of Complex Elliptically Symmetric (CES) distributions. For such non-Gaussian processes, the Fisher Information Matrix (FIM) takes a more general form than the standard Slepian–Bangs formula, which is strictly valid only for Gaussian data. As derived by Besson and Abramovich [24], the FIM for CES distributions includes corrective scaling factors that depend on the texture distribution. Our derivation of the Bayesian BCRB in Sec. IV-B will incorporate this correct statistical model, ensuring the theoretical validity of our sensing performance metric. This approach avoids model misspecification while preserving the tractability of the optimization framework.

The post-compression output combines spatial beamforming (via $\mathbf{u} \in \mathbb{C}^{N_r}$) and temporal matched filtering as:

$$r_\ell = (\mathbf{h}_{\text{pc}} \otimes \mathbf{u})^H \text{vec}(\mathbf{Y}_\ell), \tag{10}$$

where $\text{vec}(\cdot)$ vectorizes column-wise, yielding the slow-time vector $\mathbf{r} = [r_0, \ldots, r_{L-1}]^T$. Equivalently, the post-compression signal can be decomposed as:

$$r_\ell = r_\ell^{(\text{tgt})} + r_\ell^{(\text{clutter})} + r_\ell^{(\text{SI})} + r_\ell^{(\text{noise})}, \tag{11}$$

where each component is obtained by applying $(\mathbf{h}_{\text{pc}} \otimes \mathbf{u})^H$ to the corresponding term in (9). The post-compression covariance $\mathbf{R}_{\text{pc}}$ and mean $\boldsymbol{\mu}$ depend explicitly on $\mathbf{h}_{\text{pc}}$, making it a critical design variable for sensing performance (see Sec. IV-B).

IV. Performance Metrics

A. Communication Metrics

We evaluate communication performance via the signal-to-interference-plus-noise ratio (SINR) at the legitimate user Bob and the potential eavesdropper Eve. Given the transmit beamformer $\mathbf{w}$ and artificial noise covariance $\mathbf{Q}$, the received SINR at Bob is given as

$$\text{SINR}_b(\mathbf{w}, \mathbf{Q}) = \frac{|\mathbf{h}_b^{\text{H}} \mathbf{w}|^2}{\mathbf{h}_b^{\text{H}} \mathbf{Q} \mathbf{h}_b + \sigma_{b,\text{eff}}^2}, \tag{12}$$

where $\sigma_{b,\text{eff}}^2$ includes both thermal noise and residual self-interference, consistent with the radar post-compression SINR. Note that the AN covariance $\mathbf{Q}$ is designed to satisfy the Bob-null AN constraint $\mathbf{h}_b^{\text{H}} \mathbf{Q} \mathbf{h}_b = 0$ (see Sec. VI-B), ensuring that Bob experiences no AN interference.

For Eve at angle $\theta \in \Theta_e$, the SINR is expressed as:

$$\text{SINR}_e(\theta; \mathbf{w}, \mathbf{Q}) = \frac{|\mathbf{h}_e^{\text{H}}(\theta) \mathbf{w}|^2}{\mathbf{h}_e^{\text{H}}(\theta) \mathbf{Q} \mathbf{h}_e(\theta) + \sigma_{e,\text{eff}}^2(\theta)}, \tag{13}$$

where $\sigma_{b,\text{eff}}^2$ and $\sigma_{e,\text{eff}}^2(\theta)$ denote the effective noise power at Bob and Eve, respectively. The eavesdropper angular sector Θ_e represents the bearing uncertainty of potential maritime eavesdroppers, such as surveillance vessels, UAVs, or aircraft. In practice, Θ_e can be determined from coarse radar surveillance, historical threat regions, or tracking uncertainty. For example, if an adversarial vessel moves at speed v_e and is located at range R from the HAPS/LEO platform, its angular displacement over an update interval Δt is approximately $\Delta\theta \approx v_e \Delta t / R$, and the sector width can be enlarged accordingly with additional sensing or tracking margins.

The worst-case SR over Eve's angular sector Θ_e is defined as [29], [30]

$$\text{SR}_{\min}(\mathbf{w}, \mathbf{Q}) \triangleq$$
$$\min_{\theta \in \Theta_e} \left[\log_2 \left(1 + \text{SINR}_b(\mathbf{w}, \mathbf{Q})\right) - \log_2 \left(1 + \text{SINR}_e(\theta; \mathbf{w}, \mathbf{Q})\right) \right]^+, \tag{14}$$

where SINR_b and SINR_e are given in (12) and (13), respectively. Furthermore, the radar beampattern and communication directional gains toward users (as defined in Sec. III-B):

$$B_{\text{rad}}(\theta) = |\mathbf{a}_t^H(\theta) \mathbf{w}|^2, G_b = |\mathbf{h}_b^H \mathbf{w}|^2, G_e = |\mathbf{h}_e^H \mathbf{w}|^2. \tag{15}$$

B. Sensing Metrics

The post-compression radar observation is modeled as a CES random vector

$$\mathbf{r} \sim \text{CES}\big(\boldsymbol{\mu}(\boldsymbol{\xi}), \mathbf{R}_{\text{pc}}, g\big),$$

where the unknown parameter vector $\boldsymbol{\xi} = [\Re\{\alpha_t\}, \Im\{\alpha_t\}, \boldsymbol{\eta}^T]^T$ contains the complex target amplitude α_t and the target state $\boldsymbol{\eta} = [\tau_t, \theta_t, f_D]^T$. The mean vector $\boldsymbol{\mu}(\boldsymbol{\xi})$ is obtained from the post-compression processing $r_\ell = (\mathbf{h}_{\text{pc}} \otimes \mathbf{u})^H \text{vec}(\mathbf{Y}_\ell)$ applied to the 2D observation matrices $\mathbf{Y}_\ell \in \mathbb{C}^{N_r \times N}$. This CES model follows from the SIRP/K-distributed sea clutter representation, where the clutter is expressed as the product of a nonnegative texture variable and a complex Gaussian speckle component. The texture captures the heavy-tailed amplitude fluctuation of maritime clutter, while the speckle determines the scatter structure. Therefore, compared with the Gaussian Slepian–Bangs formula, the FIM under CES clutter contains a texture-dependent scaling factor.

In deriving the FIM, we assume that the post-compression scatter matrix $\mathbf{R}_{\text{pc}}$ is independent of the unknown target parameters $\boldsymbol{\eta} = [\tau_t, \theta_t, f_D]^T$. This assumption is consistent with our signal model: $\mathbf{R}_{\text{pc}}$ is determined by the sea-clutter statistics, residual self-interference, thermal noise, and the fixed pulse-compression/receive filters during each FIM evaluation, whereas the target delay, angle, and Doppler affect the likelihood through the mean response $\boldsymbol{\mu}(\boldsymbol{\xi})$. Accordingly, only the mean-response derivatives are involved in the FIM expression used here.

Under this assumption, the CES-form data FIM is given by

$$[\mathbf{J}_D]_{ij} = c_1 \, 2\Re \left\{ \frac{\partial \boldsymbol{\mu}^H}{\partial \xi_i} \mathbf{R}_{\text{pc}}^{-1} \frac{\partial \boldsymbol{\mu}}{\partial \xi_j} \right\}, \tag{16}$$

where c_1 is the texture-dependent scaling factor. For the inverse-gamma texture used in the K-distributed clutter model, $\tau \sim \text{Inv-Gamma}(\nu, \beta)$, this factor is determined by the inverse moments of the texture as $c_1 = \mathbb{E}[1/\tau^2]/(\mathbb{E}[1/\tau])^2 = (\nu + 1)/\nu$. With the default shape parameter $\nu = 2$, we obtain $c_1 = 1.5$. When $c_1 = 1$, (16) reduces to the conventional Gaussian-clutter Slepian–Bangs form.

The corresponding BFIM is

$$\mathbf{J}_B(\mathbf{w}, \mathbf{Q}, \mathbf{h}_{\text{pc}}) = \mathbb{E}_{\boldsymbol{\eta}}\big[\mathbf{J}_D(\boldsymbol{\eta}; \mathbf{w}, \mathbf{Q}, \mathbf{h}_{\text{pc}})\big] + \mathbf{J}_P, \tag{17}$$

where $\boldsymbol{\eta} \sim \mathcal{N}(\bar{\boldsymbol{\eta}}, \boldsymbol{\Sigma}_\eta)$ with $\boldsymbol{\Sigma}_\eta = \text{diag}(\sigma_\tau^2, \sigma_\theta^2, \sigma_{f_D}^2)$. The expectation $\mathbb{E}_{\boldsymbol{\eta}}[\cdot]$ is taken over this Gaussian prior, either analytically or via numerical quadrature/Monte Carlo integration. The BCRB and the D-optimal sensing metric are then given by

$$\begin{aligned} \text{BCRB}(\mathbf{w}, \mathbf{Q}, \mathbf{h}_{\text{pc}}) &= \text{diag}\big(\mathbf{J}_B^{-1}(\mathbf{w}, \mathbf{Q}, \mathbf{h}_{\text{pc}})\big), \\ \Psi(\mathbf{w}, \mathbf{Q}, \mathbf{h}_{\text{pc}}) &= \log\det \mathbf{J}_B(\mathbf{w}, \mathbf{Q}, \mathbf{h}_{\text{pc}}). \end{aligned} \tag{18}$$

Eq (16) is applied with differentiable $\boldsymbol{\mu}(\boldsymbol{\xi})$ and positive definite $\mathbf{R}_{\text{pc}}$. During each FIM evaluation, $\mathbf{R}_{\text{pc}}$ is regarded as independent of the target state $\boldsymbol{\eta}$, so that $\partial \mathbf{R}_{\text{pc}} / \partial \boldsymbol{\eta} = \mathbf{0}$. This is consistent with our model, where the delay, angle, and Doppler affect the mean target response, while the clutter, residual self-interference, thermal noise, and fixed filters determine the disturbance covariance. Although $\mathbf{R}_{\text{pc}}$ can be updated across

AO iterations or LEO slots, no covariance-derivative term is needed within a single FIM evaluation.

Then, we partition the FIM as

$$\mathbf{J} = \begin{bmatrix} \mathbf{J}_{\alpha\alpha} & \mathbf{J}_{\alpha\eta} \\ \mathbf{J}_{\eta\alpha} & \mathbf{J}_{\eta\eta} \end{bmatrix}, \quad \mathbf{J}_P = \mathrm{blkdiag}(\mathbf{0}_{2\times 2}, \mathbf{J}_{P,\eta}),$$

where $\mathbf{J}_{P,\eta}$ encodes the prior on (τ_t, θ_t, f_D), if any. Eliminating the unknown complex amplitude α_t via Schur complement yields the equivalent information for $\boldsymbol{\eta}$:

$$\mathbf{J}_{\eta|\alpha} = \mathbf{J}_{\eta\eta} - \mathbf{J}_{\eta\alpha}\mathbf{J}_{\alpha\alpha}^{-1}\mathbf{J}_{\alpha\eta}. \tag{19}$$

Under nonzero post-compression mainlobe response $\mathbf{h}_{\mathrm{pc}}^H\mathbf{s} \neq 0$ and signal-to-noise ratio (SNR) > 0, the block $\mathbf{J}_{\alpha\alpha} \succ \mathbf{0}$, so the Schur complement elimination of α_t is valid. This is because $\boldsymbol{\mu} = \alpha_t \mathbf{g}(\boldsymbol{\eta})$ with $\mathbf{g}(\boldsymbol{\eta}) \neq \mathbf{0}$, ensuring that $\mathbf{J}_{\alpha\alpha} = c_1 \cdot 2(\mathbf{g}^H \mathbf{R}_{\mathrm{pc}}^{-1}\mathbf{g})\mathbf{I}_2 \succ \mathbf{0}$. The Bayesian information matrix for $\boldsymbol{\eta}$ is $\mathbf{J}_B = \mathbf{J}_{\eta|\alpha} + \mathbf{J}_{P,\eta}$. We adopt the D-optimal criterion, i.e., $\Psi(\mathbf{w}, \mathbf{Q}, \mathbf{h}_{\mathrm{pc}}) = \log\det \mathbf{J}_B(\mathbf{w}, \mathbf{Q}, \mathbf{h}_{\mathrm{pc}})$. This minimizes the volume of the parameter confidence ellipsoid for balanced multi-parameter estimation (τ_t, θ_t, f_D).

V. Problem Formulation

ISAC systems must simultaneously illuminate maritime targets and protect confidential communication links. However, directing spatial energy toward the target sector inevitably strengthens potential eavesdroppers in overlapping angular regions, creating a fundamental sensing–secrecy trade-off. Moreover, heavy-tailed sea clutter and joint delay/angle/Doppler estimation require a principled Fisher-information treatment rather than heuristic power shaping. We address this by formulating a multi-objective transmit optimization over $(\mathbf{w}, \mathbf{Q}, \mathbf{h}_{\mathrm{pc}})$ that balances D-optimal Bayesian sensing information under SIRP clutter against worst-case secrecy performance.

A. Objective Function

We jointly optimize the transmit beamformer $\mathbf{w} \in \mathbb{C}^{N_t}$, artificial noise covariance $\mathbf{Q} \succeq 0$, and pulse compression filter $\mathbf{h}_{\mathrm{pc}} \in \mathbb{C}^N$ to balance sensing accuracy and worst-case secrecy. The beamformer shapes the spatial pattern, $\mathbf{Q}$ degrades eavesdropper reception via Bob-null structure, and $\mathbf{h}_{\mathrm{pc}}$ suppresses clutter. The objective combines the log-determinant of the BFIM $\Psi(\mathbf{w}, \mathbf{Q}, \mathbf{h}_{\mathrm{pc}}) = \log\det \mathbf{J}_B$ (sensing metric) with the worst-case SR $\mathrm{SR}_{\min}(\mathbf{w}, \mathbf{Q})$ over Eve's angular sector Θ_e (security metric), subject to beampattern constraints enforcing a flat-top mainlobe toward the target and sidelobe suppression elsewhere.

1) Sensing Metric: We adopt the sensing metric Ψ defined in (18), which provides a D-optimal criterion for multi-parameter estimation under the BCRB framework:

$$\Psi(\mathbf{w}, \mathbf{Q}, \mathbf{h}_{\mathrm{pc}}) = \log\det(\mathbf{J}_B(\mathbf{w}, \mathbf{Q}, \mathbf{h}_{\mathrm{pc}})), \tag{20}$$

where $\mathbf{J}_B$ is the BFIM. A larger Ψ yields a smaller BCRB, thereby achieving better sensing performance.

2) Security Metric: We evaluate security via the *worst-case SR* over Eve's angular sector Θ_e:

$$\mathrm{SR}_{\min}(\mathbf{w}, \mathbf{Q}) = \min_{\theta \in \Theta_e} \mathrm{SR}(\mathbf{w}, \mathbf{Q}; \theta), \tag{21}$$

where $\mathrm{SR}(\mathbf{w}, \mathbf{Q}; \theta)$ is the instantaneous SR at angle θ defined in (14). This worst-case formulation ensures robustness against angular uncertainty in Eve's location, which is the practically relevant case in maritime scenarios.[5]

B. Weighted-Sum Optimization Problem

We adopt a weighted-sum formulation that balances sensing and security objectives. To ensure meaningful trade-off analysis, we normalize both objectives to comparable scales using endpoint values. We define the normalization endpoints via two single-objective optimization problems over the same feasible set $\mathcal{X}_{\mathrm{SOC}}^{\mathrm{IA}}$ (detailed in Sec. VI-A):

$$\Psi_0 = \max_{\mathbf{w}, \mathbf{Q}\succeq 0, \mathbf{h}_{\mathrm{pc}}, t} \Psi(\mathbf{w}, \mathbf{Q}, \mathbf{h}_{\mathrm{pc}}) \quad \text{s.t. } (\mathbf{w}, \mathbf{Q}, t) \in \mathcal{X}_{\mathrm{SOC}}^{\mathrm{IA}}, \tag{22}$$

$$\mathrm{SR}_0 = \max_{\mathbf{w}, \mathbf{Q}\succeq 0, \mathbf{h}_{\mathrm{pc}}, t} \mathrm{SR}_{\min}(\mathbf{w}, \mathbf{Q}) \quad \text{s.t. } (\mathbf{w}, \mathbf{Q}, t) \in \mathcal{X}_{\mathrm{SOC}}^{\mathrm{IA}}. \tag{23}$$

These are computed once per experimental setup and cached. The normalized objectives are:

$$\widehat{\Psi} = \frac{\Psi}{\Psi_0}, \qquad \widehat{\mathrm{SR}}_{\min} = \frac{\mathrm{SR}_{\min}}{\mathrm{SR}_0}. \tag{24}$$

For multi-slot LEO scenarios, endpoints aggregate across time slots: $\Psi_0^{\mathrm{LEO}} = \frac{1}{|\mathcal{T}|}\sum_{t\in\mathcal{T}} \Psi_0(t)$ and $\mathrm{SR}_0^{\mathrm{LEO}} = \min_{t\in\mathcal{T}} \mathrm{SR}_0(t)$.

Towards this end, the optimization problem is formulated as **Problem (P):**

$$\max_{\mathbf{w}, \mathbf{Q}\succeq 0, \mathbf{h}_{\mathrm{pc}}, t} \quad \alpha_{\mathrm{ws}} \widehat{\Psi}(\mathbf{w}, \mathbf{Q}, \mathbf{h}_{\mathrm{pc}}) + (1-\alpha_{\mathrm{ws}})\widehat{\mathrm{SR}}_{\min}(\mathbf{w}, \mathbf{Q}) \tag{25a}$$

$$\text{s.t.} \quad (\mathbf{w}, \mathbf{Q}, t) \in \mathcal{X}_{\mathrm{SOC}}^{\mathrm{IA}}, \tag{25b}$$

where $\alpha_{\mathrm{ws}} \in [0, 1]$ is the trade-off factor, i.e., $\alpha_{\mathrm{ws}} = 1$ prioritizes sensing, $\alpha_{\mathrm{ws}} = 0$ prioritizes security, and intermediate values balance both objectives. The pulse compression filter $\mathbf{h}_{\mathrm{pc}}$ is jointly optimized with $(\mathbf{w}, \mathbf{Q})$ via alternating optimization: while the feasible set $\mathcal{X}_{\mathrm{SOC}}^{\mathrm{IA}}$ constrains only $(\mathbf{w}, \mathbf{Q}, t)$, the $\mathbf{h}_{\mathrm{pc}}$ update is decoupled and solved via closed-form regularized MVDR, which monotonically increases the sensing objective Ψ without violating any constraints.

The feasible set $\mathcal{X}_{\mathrm{SOC}}^{\mathrm{IA}}$ enforces power budget, beampattern shaping, and sidelobe suppression via SOCP-compatible constraints, which is written as

$$\begin{aligned} \mathcal{X}_{\mathrm{ideal}} \triangleq \Big\{ (\mathbf{w}, \mathbf{Q}, t) \;\Big|\; & \|\mathbf{w}\|_2^2 + \mathrm{tr}(\mathbf{Q}) \le 1,\ t \le |\mathbf{a}_t^H(\theta_0)\mathbf{w}|, \\ & (1-\alpha_{\mathrm{ml}})t \;\le\; |\mathbf{a}_t^H(\theta)\mathbf{w}| \;\le\; (1+\alpha_{\mathrm{ml}})t,\ \forall \theta \in \Theta_{\mathrm{ml}}, \\ & |\mathbf{a}_t^H(\theta_p)\mathbf{w}| \;\le\; \eta\, t,\ \forall \theta_p \in \Theta_{\mathrm{sl}} \Big\}. \end{aligned} \tag{26}$$

where $t \in \mathbb{R}^+$ is a scaling parameter that serves as a lower bound on the mainlobe amplitude at θ_0, and $\eta \in (0, 1)$ denotes

[5]We consider an angular-sector uncertainty model: Eve's AoA lies in a known sector Θ_e, but the exact angle is unknown. When the instantaneous CSI of Eve is available, the sector minimization in (21) is removed and $\mathrm{SR}_{\min}$ reduces to the instantaneous SR. This modeling choice balances robustness and tractability while remaining compatible with the weighted-sum formulation below.

the mainlobe-to-sidelobe suppression ratio. The relation to a desired gap G (in dB) is given by $\eta = 10^{-G/20}$. The constraint $t \le |\mathbf{a}_t^H(\theta_0)\mathbf{w}|$ ensures that t does not exceed the actual mainlobe response, while the relative constraints $(1-\alpha_{\text{ml}})t \le |\mathbf{a}_t^H(\theta)\mathbf{w}| \le (1+\alpha_{\text{ml}})t$ and $|\mathbf{a}_t^H(\theta_p)\mathbf{w}| \le \eta t$ enforce that the beampattern magnitude lies within a relative tolerance α_{ml} of the scaling parameter t over the mainlobe region Θ_{ml}, and is suppressed below ηt in the sidelobe region Θ_{sl} [6]. The optimization over t allows the algorithm to balance between mainlobe flatness and sidelobe suppression. However, the constraints in (26) are nonconvex, which will be approximated in the following.

VI. Convex Reformulation and Alternating Optimization

Problem (P) is nonconvex due to the nonlinear coupling of $(\mathbf{w}, \mathbf{Q}, \mathbf{h}_{\text{pc}})$ in the BCRB objective and the fractional quadratic forms in the secrecy rate. We address this through: (i) reformulating the ideal beampattern constraints as a convex inner approximation via phase-wedge decomposition, yielding a second-order cone programming (SOCP)-compatible feasible set, and (ii) developing an AO algorithm that decouples the terms in the objective function and admits convex subproblem solutions. This section presents the generic AO framework, while platform-specific instantiations (LEO multi-slot robustness, Doppler/ICI compensation) are presented in Section VII.

A. SOCP Inner Approximation

To obtain a tractable convex formulation, we replace the nonconvex constraints in (26) with an SOCP-compatible inner approximation, yielding the following convex program:

$$
\begin{aligned}
\max_{\mathbf{w},\mathbf{Q}\succeq 0,t}\quad & \alpha_{\text{ws}}\,\widehat{\Psi}(\mathbf{w},\mathbf{Q}) + (1-\alpha_{\text{ws}})\,\widehat{\text{SR}}_{\min}(\mathbf{w},\mathbf{Q}) \\
\text{s.t.}\quad & \Im\{\mathbf{a}_t^H(\theta_0)\mathbf{w}\} = 0, \\
& \Re\{\mathbf{a}_t^H(\theta_0)\mathbf{w}\} \ge t, \\
& \left\| \begin{bmatrix} \Re\{\mathbf{a}_t^H(\theta)\mathbf{w}\} \\ \Im\{\mathbf{a}_t^H(\theta)\mathbf{w}\} \end{bmatrix} \right\|_2 \le (1+\alpha_{\text{ml}})t,\ \forall\theta\in\Theta_{\text{ml}}, \\
& \Re\{\mathbf{a}_t^H(\theta)\mathbf{w}\} \ge (1-\alpha_{\text{ml}})t\cos\delta,\ \forall\theta\in\Theta_{\text{ml}}, \\
& -\tan\delta\,\Re\{\mathbf{a}_t^H(\theta)\mathbf{w}\} \le \Im\{\mathbf{a}_t^H(\theta)\mathbf{w}\} \\
& \qquad\qquad \le \tan\delta\,\Re\{\mathbf{a}_t^H(\theta)\mathbf{w}\},\ \forall\theta\in\Theta_{\text{ml}}, \\
& \left\| \begin{bmatrix} \Re\{\mathbf{a}_t^H(\theta_p)\mathbf{w}\} \\ \Im\{\mathbf{a}_t^H(\theta_p)\mathbf{w}\} \end{bmatrix} \right\|_2 \le \eta\, t,\ \forall\theta_p\in\Theta_{\text{sl}}, \\
& \|\mathbf{w}\|_2^2 + \text{tr}(\mathbf{Q}) \le 1, \quad t\ge 0.
\end{aligned}
\tag{27}
$$

where $\delta \in (0, \pi/2)$ denotes the half-angle of the phase-wedge used in the inner approximation.

[6]The mainlobe region Θ_{ml} is intentionally designed to be wide (typically spanning $\pm\theta_{3\text{dB}}$ around the mainlobe center), rather than a narrow peak. This design choice serves two purposes: (i) it ensures robust communication performance by maintaining a relatively flat response over a wide angular range, reducing sensitivity to target/user location uncertainty; (ii) it allows the optimization algorithm to have sufficient degrees of freedom to simultaneously satisfy both communication and sensing objectives. The constraint $|\mathbf{a}_t^H(\theta)\mathbf{w}| \in [(1-\alpha_{\text{ml}})t, (1+\alpha_{\text{ml}})t]$ for $\theta\in\Theta_{\text{ml}}$ enforces that the mainlobe response remains within a relative tolerance α_{ml} of the reference amplitude t, which is more general than requiring a strictly flat response.

Problem (27) defines the feasible set $\mathcal{X}_{\text{SOC}}^{\text{IA}}$ as the intersection of linear, quadratic, and second-order cone (SOC) constraints, which is convex. The phase anchor constraint $\Im\{\mathbf{a}_t^H(\theta_0)\mathbf{w}\} = 0$ eliminates global phase ambiguity and enables real-valued scaling via t. The nonconvex lower-envelope constraint $|\mathbf{a}_t^H(\theta)\mathbf{w}| \ge (1-\alpha_{\text{ml}})t$ is conservatively approximated by the phase-wedge constraints, which are linear in the real and imaginary parts of $\mathbf{a}_t^H(\theta)\mathbf{w}$. The resulting SOCP-compatible problem can be efficiently solved using standard convex optimization solvers.

B. Alternating Optimization

Given the convex inner feasible set $\mathcal{X}_{\text{SOC}}^{\text{IA}}$ in Sec. VI-A, we solve (27) by AO over three blocks $(\mathbf{w}, \mathbf{Q}, \mathbf{h}_{\text{pc}})$. Each block admits a tractable update: (i) a projected-gradient step for $\mathbf{w}$ with SOCP projection; (ii) a null-space shaping step for $\mathbf{Q}$ solved via epigraph bisection over a semidefinite programming (SDP) feasibility test; and (iii) a closed-form regularized MVDR update for $\mathbf{h}_{\text{pc}}$. The objective is nondecreasing across iterations, ensuring monotonic convergence to a first-order stationary point. Initialization uses a Linearly Constrained Minimum Variance (LCMV) solution for $\mathbf{w}$ (followed by power normalization), a Bob-null $\mathbf{Q}$, and a matched-filter seed for $\mathbf{h}_{\text{pc}}$; stopping uses a relative objective change $< 10^{-3}$ or a cap of 20 iterations.

1) $\mathbf{w}$-Update: We first fix $(\mathbf{Q}, \mathbf{h}_{\text{pc}})$. Let $s_b(\mathbf{w}) = |\mathbf{h}_b^H\mathbf{w}|^2$ and $s_{e,j}(\mathbf{w}) = |\mathbf{h}_{e,j}^H\mathbf{w}|^2$ for each discretized pair $j \leftrightarrow (\theta, \Delta f) \in \Theta_e \times \mathcal{F}$, where j is the index of the $(\theta, \Delta f)$ grid point in $\Theta_e \times \mathcal{F}$. Since $\mathbf{Q}$ is fixed, the SINR denominators are constants: $\alpha_b \triangleq (\mathbf{h}_b^H\mathbf{Q}\mathbf{h}_b + \sigma_{b,\text{eff}}^2)^{-1}$ and $\alpha_{e,j} \triangleq (\mathbf{h}_{e,j}^H\mathbf{Q}\mathbf{h}_{e,j} + \sigma_{e,\text{eff}}^2(j))^{-1}$. Define

$$
\begin{aligned}
F_b(\mathbf{w}) &= \log_2\big(1+\alpha_b s_b(\mathbf{w})\big), \\
F_{e,j}(\mathbf{w}) &= \log_2\big(1+\alpha_{e,j} s_{e,j}(\mathbf{w})\big).
\end{aligned}
\tag{28}
$$

To smooth the $\min_{(\theta,\Delta f)}$ in the secrecy term, use $\psi_\tau(\{F_{e,j}\}) = \tau\log\sum_j \exp(F_{e,j}/\tau)$ with temperature parameter $\tau > 0$ (smaller τ yields tighter approximation to $\max_j$). Maximize the smoothed lower bound

$$
\widetilde{\text{SR}}_{\min}(\mathbf{w}) \ \triangleq\ F_b(\mathbf{w}) - \psi_\tau\big(\{F_{e,j}(\mathbf{w})\}\big), \tag{29}
$$

where the outer $[\cdot]^+$ is omitted without affecting the maximizer.

With $\mathbf{H}_b = \mathbf{h}_b\mathbf{h}_b^H$ and $\mathbf{H}_{e,j} = \mathbf{h}_{e,j}\mathbf{h}_{e,j}^H$, we have

$$
\nabla_{\mathbf{w}}F_b = \frac{\alpha_b}{\ln 2}\frac{\mathbf{H}_b\mathbf{w}}{1+\alpha_b s_b}, \nabla_{\mathbf{w}}F_{e,j} = \frac{\alpha_{e,j}}{\ln 2}\frac{\mathbf{H}_{e,j}\mathbf{w}}{1+\alpha_{e,j}s_{e,j}}. \tag{30}
$$

Let $\pi_j = \exp(F_{e,j}/\tau)\big/\sum_\ell \exp(F_{e,\ell}/\tau)$ denote the softmax weights. Then

$$
\nabla_{\mathbf{w}}\widetilde{\text{SR}}_{\min} = \nabla_{\mathbf{w}}F_b - \sum_j \pi_j\,\nabla_{\mathbf{w}}F_{e,j}. \tag{31}
$$

For the sensing term, we use the Fréchet derivative of the log-det, i.e., for any $\mathbf{J}_B \succ 0$, the directional derivative of $f(\mathbf{J}) = \log\det\mathbf{J}$ in direction $\Delta\mathbf{J}$ is $Df[\mathbf{J}_B](\Delta\mathbf{J}) = \text{tr}(\mathbf{J}_B^{-1}\Delta\mathbf{J})$. Applying the chain rule to $\mathbf{J}_B(\mathbf{w})$ gives $\dfrac{\partial\Psi}{\partial w_k} = \text{tr}\big(\mathbf{J}_B^{-1}\dfrac{\partial\mathbf{J}_B}{\partial w_k}\big)$. The total gradient is $\mathbf{g} = \alpha_{\text{ws}}\nabla_{\mathbf{w}}\widehat{\Psi} + (1-\alpha_{\text{ws}})\nabla_{\mathbf{w}}\widehat{\widetilde{\text{SR}}}_{\min}$. Take an Armijo backtracking ascent step $\tilde{\mathbf{w}} \leftarrow \mathbf{w} + \gamma\mathbf{g}$.

Then, we project $\tilde{\mathbf{w}}$ onto $\mathcal{X}_{\mathrm{SOC}}^{\mathrm{IA}}$ by solving the following SOCP:

$$
\begin{aligned}
\min_{\mathbf{w},t}\ & \|\mathbf{w}-\tilde{\mathbf{w}}\|_2^2 \\
\text{s.t. } & \|\mathbf{w}\|_2^2 \le 1-\mathrm{tr}(\mathbf{Q}),\ \Im\{\mathbf{a}^H(\theta_0)\mathbf{w}\}=0,\ \Re\{\mathbf{a}^H(\theta_0)\mathbf{w}\}\ge t,\ t\ge 0, \\
& \left\|\left[\Re\{\mathbf{a}^H(\theta)\mathbf{w}\},\ \Im\{\mathbf{a}^H(\theta)\mathbf{w}\}\right]^T\right\|_2 \le (1+\alpha_{\mathrm{ml}})t,\ \forall\theta\in\Theta_{\mathrm{ml}}, \\
& \Re\{\mathbf{a}^H(\theta)\mathbf{w}\} \ge (1-\alpha_{\mathrm{ml}})t\cos\delta, \\
& -\tan\delta\,\Re\{\cdot\} \le \Im\{\cdot\} \le \tan\delta\,\Re\{\cdot\},\ \forall\theta\in\Theta_{\mathrm{ml}}, \\
& \left\|\left[\Re\{\mathbf{a}^H(\theta_p)\mathbf{w}\},\ \Im\{\mathbf{a}^H(\theta_p)\mathbf{w}\}\right]^T\right\|_2 \le \eta t,\ \forall\theta_p\in\Theta_{\mathrm{sl}}.
\end{aligned}
\tag{32}
$$

2) $\mathbf{Q}$-Update: Fix $(\mathbf{w},\mathbf{h}_{\mathrm{pc}})$ and write $\mathbf{Q}=\mathbf{U}_\perp\mathbf{\Lambda}\mathbf{U}_\perp^H$, where $\mathbf{U}_\perp$ spans Bob's null-space and $\mathbf{\Lambda}\succeq\mathbf{0}$ with $\mathrm{tr}(\mathbf{\Lambda})\le 1-\|\mathbf{w}\|_2^2$. Define the worst-case Eve SINR

$$
\Gamma(\mathbf{\Lambda}) \triangleq \max_j \ \frac{|\mathbf{h}_{e,j}^H\mathbf{w}|^2}{\mathbf{h}_{e,j}^H\mathbf{U}_\perp\mathbf{\Lambda}\mathbf{U}_\perp^H\mathbf{h}_{e,j}+\sigma_{e,\mathrm{eff}}^2(j)}.
$$

Minimize $\Gamma(\mathbf{\Lambda})$ via epigraph bisection on γ: for a trial γ, check feasibility of

$$
\begin{aligned}
\text{find}\quad & \mathbf{\Lambda} \\
\text{s.t.}\quad & \mathrm{tr}\big(\mathbf{A}_j\mathbf{\Lambda}\big) \ \ge\ |\mathbf{h}_{e,j}^H\mathbf{w}|^2/\gamma - \sigma_{e,\mathrm{eff}}^2(j), \quad \forall j, \\
& \mathbf{\Lambda}\succeq\mathbf{0}, \qquad \mathrm{tr}(\mathbf{\Lambda})\le 1-\|\mathbf{w}\|_2^2,
\end{aligned}
\tag{33}
$$

with $\mathbf{A}_j \triangleq \mathbf{U}_\perp^H\mathbf{h}_{e,j}\mathbf{h}_{e,j}^H\mathbf{U}_\perp\succeq\mathbf{0}$. Bisection shrinks the interval until the smallest feasible $\gamma^\star$ is found; the corresponding $\mathbf{\Lambda}^\star$ (optionally constrained to be diagonal for numerical robustness) yields the AN update.

3) Pulse-Compression Update (Closed-Form Regularized MVDR): With $(\mathbf{w},\mathbf{Q})$ fixed, form $\mathbf{R}_{\mathrm{pc}}$ from the current clutter+noise statistics and let $\mathbf{s}$ be the target fast-time signature. We update the pulse compression filter via regularized Minimum Variance Distortionless Response (MVDR) [46]

$$
\mathbf{h}_{\mathrm{pc}} \leftarrow \frac{(\mathbf{R}_{\mathrm{pc}}+\varepsilon\mathbf{I})^{-1}\mathbf{s}}{\mathbf{s}^H(\mathbf{R}_{\mathrm{pc}}+\varepsilon\mathbf{I})^{-1}\mathbf{s}}, \qquad \varepsilon>0,
\tag{34}
$$

implemented via Cholesky (or conjugate gradients) to avoid explicit inversion. This step increases the sensing objective Ψ.

For clarity, the complete alternating optimization procedure is summarized in Algorithm 1.

C. Complexity Analysis

The per-iteration complexity of the proposed AO algorithm is dominated by solving the SOCP for the $\mathbf{w}$-update and the SDP feasibility checks within the bisection-based $\mathbf{Q}$-update, yielding an overall cost of $O\big(N_t^3M+N^3\big)$ per iteration, where N_t is the number of transmit antennas, N is the number of fast-time samples, and M denotes the total number of angular and Doppler grid points across mainlobe, sidelobe, and eavesdropper sectors. In practice, the algorithm converges in around 5 iterations under typical maritime scenarios, and warm-starting across LEO time slots further reduces the iteration count, making the approach computationally tractable for real-time HAPS and LEO beamforming applications.

Algorithm 1 AO Algorithm for Solving Problem (P)

Require: System parameters: N_t, $\mathbf{h}_b$, Θ_e, $\mathcal{F}$, α_{ws}, $P_{\max}$, τ, δ, α_{ml}, η
Require: Convergence tolerance $\varepsilon_{\mathrm{tol}}=10^{-3}$, maximum iterations $K_{\max}=20$
Ensure: Optimized beamforming vector $\mathbf{w}^\star$, AN covariance $\mathbf{Q}^\star$, pulse compression filter $\mathbf{h}_{\mathrm{pc}}^\star$

```
Initialization:
Compute LCMV solution for w^(0) and normalize to satisfy ||w^(0)||_2^2 ≤ P_max
Compute Bob's null-space basis U_⊥ via QR decomposition of h_b
Initialize Q^(0) = U_⊥ Λ^(0) U_⊥^H with Λ^(0) = (P_max − ||w^(0)||_2^2) I_{N_t−1} / (N_t − 1)
Initialize h_pc^(0) as matched filter: h_pc^(0) = s/||s||_2
Compute initial objective Φ^(0) = α_ws Ψ̂(w^(0), Q^(0)) + (1 − α_ws) SR̂_min(w^(0), Q^(0))
for k = 1, 2, ..., K_max do
    Step 1: w-Update (Sec. VI-B1)
    Fix Q^(k−1), h_pc^(k−1)
    Compute gradient g^(k) = α_ws ∇_w Ψ̂(w^(k−1)) + (1 − α_ws) ∇_w SR̃_min(w^(k−1))
    Armijo backtracking: w̃^(k) ← w^(k−1) + γ g^(k)
    Project onto X_SOC^IA via SOCP (32): w^(k) ← Π_X(w̃^(k))
    Step 2: Q-Update (Sec. VI-B2)
    Fix w^(k), h_pc^(k−1)
    Bisection on γ ∈ [γ_min, γ_max]:
        Find smallest γ* such that SDP (33) is feasible
    Update Λ^(k) ← Λ* from feasibility test
    Reconstruct Q^(k) = U_⊥ Λ^(k) U_⊥^H
    Step 3: h_pc-Update (Sec. VI-B3)
    Fix w^(k), Q^(k)
    Compute clutter covariance R_pc from current (w^(k), Q^(k))
    Regularized MVDR: h_pc^(k) = (R_pc + εI)^(−1) s / (s^H (R_pc + εI)^(−1) s)
    Convergence Check:
    Compute Φ^(k) = α_ws Ψ̂(w^(k), Q^(k)) + (1 − α_ws) SR̂_min(w^(k), Q^(k))
    if |Φ^(k) − Φ^(k−1)| / |Φ^(k−1)| < ε_tol then
        break
    end if
end for
return w* = w^(k), Q* = Q^(k), h_pc* = h_pc^(k)
```

VII. Extension: LEO Slotting and Doppler/ICI Robustification

The preceding framework assumes quasi-stationary geometry, applicable to HAPS where Doppler shifts are negligible ($|\Delta f|\ll 1/T_r$). LEO satellites, with orbital velocities of ≈ 7.5 km/s, induce Doppler shifts of $\pm$(5–15) kHz at typical carrier frequencies, creating ICI and time-varying geometry. We extend the framework via per-slot parameterization: each time slot is treated as an independent instance of Problem (P), with LEO-specific effects (Doppler, ICI, angular drift) absorbed into slot-dependent effective noise and uncertainty sets.

The AO structure presented in Sec. VI-B remains unchanged, enabling warm-start across slots and unified treatment of HAPS and LEO scenarios.

A. Motivation and Design Philosophy

While HAPS platforms provide quasi-stationary coverage for maritime ISAC, LEO satellites offer complementary benefits: global coverage, polar accessibility, and natural time diversity from orbital motion. Their high mobility, however, introduces Doppler/ICI impairments and fast channel dynamics that necessitate extending the baseline HAPS framework.

We identify three key LEO-specific challenges:

1) Doppler-induced ICI: LEO orbital velocities induce carrier frequency offsets (CFO) of $\pm(5\text{–}15)$ kHz, far exceeding the negligible residual offsets in HAPS scenarios. Such CFO spreads energy across subcarriers in OFDM-based waveforms, creating inter-carrier interference that degrades both communication and sensing performance.
2) Time-varying geometry: LEO links exhibit rapid angular drift (typically $0.1°$–$0.5°$ per second) and channel gain variations due to changing slant range and atmospheric conditions, motivating a slot-wise adaptation strategy.
3) Algorithmic consistency: We preserve the AO structure and incorporate LEO-specific impairments into per-slot effective noise terms and uncertainty sets, rather than redesigning the optimization algorithm.

Fig. 1 illustrates the impact of residual Doppler frequency offset Δf on the effective signal-to-interference-plus-noise ratio (SINR) and quadrature phase-shift keying (QPSK) bit error rate (BER) of an uncompensated LEO link. In contrast to the ICI-free HAPS baseline, whose effective SINR remains insensitive to Δf, the uncompensated LEO link experiences a rapid SINR reduction as $|\Delta f|$ increases, accompanied by a corresponding increase in BER. At moderate-to-large Doppler offsets, the effective SINR approaches or falls below the QPSK demodulation threshold, while the BER exceeds the prescribed reliability level. These results highlight the significant performance degradation caused by Doppler-induced inter-carrier interference (ICI) and motivate the ICI-aware effective-noise modeling and slot-wise Doppler-robust parameterization developed in the following subsections.

B. LEO Signal Model and Slot-Based Design

1) Slot-Based Parameterization: To handle time-varying LEO geometry while maintaining algorithmic consistency with the HAPS framework, we adopt a multi-slot parameterization strategy. Each satellite pass is partitioned into $|\mathcal{T}|$ discrete time slots indexed by $t \in \mathcal{T}$, each with duration T_{slot}. Within each slot, the geometry parameters Bob's angle $\theta_b(t)$, target angle $\theta_t(t)$, Eve's angular sector $\Theta_e(t)$, and channel gains $\{\beta_b(t), \beta_e(t)\}$ are treated as quasi-static and updated between slots via ephemeris predictions.

Note that the proposed Bob-null AN design implicitly assumes quasi-static knowledge of Bob's channel $\mathbf{h}_b(t)$ within each slot, which is reasonable when the dominant LoS geometry varies slowly compared with T_{slot} (e.g., the default $T_{\text{slot}} = 10$ s). Let $\Delta\theta_b$ denote the within-slot change of Bob's bearing (in radians). The corresponding phase mismatch across the ULA can be approximated as

$$\Delta\phi \approx 2\pi \frac{d}{\lambda} \Delta\theta_b, \tag{35}$$

so for typical maritime vessel speeds and slot durations, $\Delta\phi$ is small and the injected AN remains approximately orthogonal to Bob's channel. The resulting AN leakage (and SINR degradation) is of order $\mathcal{O}(\|\Delta\mathbf{h}_b\|^2)$ under small CSI errors, hence having minimal impact on the worst-case secrecy rate. If significantly longer slots or higher mobility are considered, more frequent CSI updates or predictive channel tracking may be required.

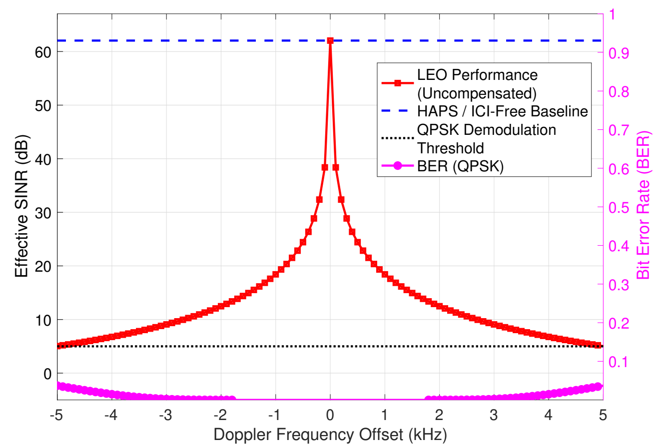

Fig. 1. Impact of Doppler frequency offset Δf on effective SINR and QPSK BER under LEO-induced ICI. Compared with the ICI-free HAPS baseline, the uncompensated LEO link degrades rapidly as $|\Delta f|$ increases, motivating the ICI-aware effective-noise model. Parameters: $N_t = 16$, $|\Theta_e| = 3°$.

2) Normalized CFO and ICI Kernel: We adopt an OFDM baseband abstraction where the residual Doppler frequency offset $\Delta f(t)$ induces ICI via spectral leakage across subcarriers. Let $\Delta f_{\text{sc}} = 1/T_u$ denote the subcarrier spacing, where T_u is the useful OFDM symbol duration. We define the normalized CFO as

$$\varepsilon \triangleq \frac{\Delta f}{\Delta f_{\text{sc}}}, \tag{36}$$

which quantifies the Doppler offset in units of subcarrier spacing. For LEO scenarios with $\Delta f \in [-15, +15]$ kHz and typical $\Delta f_{\text{sc}} = 15$ kHz (LTE-like parameters), we have $\varepsilon \in [-1, +1]$.

The ICI power leakage from subcarrier k to the reference subcarrier (indexed as 0) is characterized by the standard sinc-squared kernel[7]:

$$\kappa[k;\varepsilon] = \left| \frac{\sin(\pi(\varepsilon - k))}{\pi(\varepsilon - k)} \right|^2 = |\text{sinc}(\varepsilon - k)|^2, \tag{37}$$

where $\text{sinc}(x) \triangleq \sin(\pi x)/(\pi x)$. This kernel quantifies the fractional power leakage for a normalized CFO of ε [47].

[7]This kernel assumes equal power allocation across subcarriers.

3) Effective Noise Construction: The effective noise power at Eve's receiver, accounting for thermal noise σ_0^2, residual self-interference σ_{SI}^2, and ICI, is:

$$\sigma_{e,\text{eff}}^2(t,\theta,\varepsilon) = \sigma_0^2 + \sigma_{\text{SI}}^2 + \sum_{k\neq 0} \kappa[k;\varepsilon]\cdot P_{\text{TX}}\cdot ||\mathbf{h}_e(\theta)||^2, \quad (38)$$

where $P_{\text{TX}} = \|\mathbf{w}\|_2^2 + \text{tr}(\mathbf{Q})$ is the total transmit power and $||\mathbf{h}_e(\theta)||^2$ accounts for the channel-dependent attenuation of ICI at Eve's location. The ICI term represents power leakage from adjacent subcarriers caused by Doppler-induced CFO. Similarly, Bob's effective noise is $\sigma_{b,\text{eff}}^2(t,\varepsilon)$, computed with Bob-specific channel parameters. All power terms are in linear scale unless explicitly noted otherwise.

The ICI term in (38) is interpreted as additional receiver-side disturbance caused by Doppler-induced spectral leakage from neighboring subcarriers. Since these leaked symbols are not decoded in the considered subcarrier and are not controllable by the beamformer of the current narrowband subproblem, we absorb their aggregate power into the effective noise variance. This approximation keeps the LEO formulation compatible with the HAPS AO algorithm: Doppler changes only the slot-dependent noise levels and uncertainty grid, while the beamforming, AN, and pulse-compression updates remain unchanged.

It is noted that the resulting secrecy guarantee is with respect to this effective noise model. For each Doppler grid point, the design maximizes the worst-case secrecy rate after accounting for the ICI power as an additional disturbance. This provides a tractable robust-design metric when the ICI is not explicitly decoded. However, it is not an exact secrecy-capacity characterization of a full multicarrier LEO link with structured ICI or joint subcarrier processing. Such waveform-level secrecy analysis is beyond the scope of this work and is left for future investigation.

Lemma 1 (Conservativeness of ICI-as-Noise Approximation)**.** *Treating ICI as additive Gaussian noise yields a conservative lower bound on the achievable secrecy rate [48].*

Proof. See Appendix A. □

C. Slot-Wise Robust Optimization Problem

For each time slot $t \in \mathcal{T}$, we solve an independent instance of Problem (P) from Sec. V with slot-specific parameters $\{\theta_b(t), \theta_t(t), \Theta_e(t), \beta_b(t), \beta_e(t)\}$ and effective noise terms from (38). The key modification is the worst-case secrecy rate, which now minimizes over both angular uncertainty $\Theta_e(t)$ and Doppler uncertainty $\mathcal{F}$:

$$\text{SR}_{\min}(t) = \min_{\theta\in\Theta_e(t)} \min_{\varepsilon\in\mathcal{F}} \text{SR}(\mathbf{w}(t), \mathbf{Q}(t); \theta, \varepsilon), \quad (39)$$

where $\mathcal{F} = \{\varepsilon_1, \ldots, \varepsilon_{|\mathcal{F}|}\}$ is a discrete grid spanning the expected normalized CFO range. For typical LEO scenarios with $\Delta f \in [-5, +5]$ kHz and $\Delta f_{\text{sc}} = 15$ kHz, we use $\mathcal{F} = \{-0.33, -0.27, \ldots, +0.33\}$ with $|\mathcal{F}| = 11$ points and grid spacing $\delta_{\mathcal{F}} = 0.067$ (corresponding to 1 kHz in absolute frequency). The sensing metric $\Psi(t) = \Psi(\mathbf{w}(t), \mathbf{Q}(t), \mathbf{h}_{\text{pc}}(t))$ retains its BCRB form from Sec. IV-B, as the sensing performance is primarily affected by spatial beamforming and pulse compression rather than Doppler offset.

Proposition 1 (Doppler Grid Discretization Error)**.** *The secrecy rate $SR(\mathbf{w}, \mathbf{Q}; \theta, \varepsilon)$ is Lipschitz continuous in the normalized CFO ε with Lipschitz constant L_{SR} bounded by the composition of Lipschitz constants of the ICI kernel, effective noise, and logarithmic SINR terms.*

Proof. See Appendix B. □

Remark 1 (Tightness of Discretization Error Bound)**.** *For the default Doppler grid $|\mathcal{F}| = 11$ with spacing $\delta_{\mathcal{F}} = 1$ kHz, Proposition 1 establishes a theoretical upper bound $L_{SR}\cdot\delta_{\mathcal{F}} \approx$ 0.3–0.7 bps/Hz. However, numerical validation in Sec. VIII demonstrates that the empirical discretization error is typically < 0.01 bps/Hz, representing a gap between theory and practice. This conservatism arises because the proof employs worst-case bounds at multiple stages: the ICI summation in Step 2 assumes all $K_{\max}$ subcarrier terms contribute maximally, whereas the sinc-squared kernel exhibits exponential decay for $|k| > 2$; the SINR composition in Step 3 assumes simultaneous maximization of both Bob and Eve terms, which the optimization structure precludes; and the effective noise denominator uses $\sigma_{\min}^2$, whereas typical operating points have $\sigma_{e,\text{eff}}^2 \gg \sigma_{\min}^2$. These conservative assumptions are inherent to worst-case analysis and do not diminish the theoretical guarantees, which remain valid for all feasible parameter ranges.*

D. Algorithmic Implementation

The alternating optimization framework from Sec. VI-B applies to each LEO slot with two slot-specific adaptations:

1) Bob-Null Space Update: Recompute $\mathbf{U}_\perp(t)$ per slot from the instantaneous Bob channel $\mathbf{h}_b(t) = \sqrt{\beta_b(t)}\mathbf{a}_t(\theta_b(t))$ via QR decomposition, then optimize $\mathbf{Q}(t) = \mathbf{U}_\perp(t)\mathbf{\Lambda}(t)\mathbf{U}_\perp^H(t)$ using the slot-dependent effective noise $\sigma_{e,\text{eff}}^2(t,\theta,\varepsilon)$ from (38).
2) Doppler-Aware Secrecy Optimization: Extend the $\mathbf{w}$-update grid from Θ_e to $\Theta_e(t)\times\mathcal{F}$, yielding $|\Theta_e|\times|\mathcal{F}|$ evaluation points per iteration. The log-sum-exp smoothing with temperature parameter τ remains unchanged. Per-iteration cost scales by $|\mathcal{F}|$ relative to HAPS but remains tractable.

To exploit temporal correlation across consecutive slots, we initialize slot $t+1$ using the converged solution from slot t:

$$\left(\mathbf{w}_{t+1}^{(0)}, \mathbf{Q}_{t+1}^{(0)}, \mathbf{h}_{\text{pc},t+1}^{(0)}\right) = \left(\mathbf{w}_t^\star, \mathbf{Q}_t^\star, \mathbf{h}_{\text{pc},t}^\star\right), \quad (40)$$

where the superscript (0) denotes the initial iterate for slot $t+1$, and $\star$ denotes the converged solution from slot t. If angular variations exceed a threshold—specifically, if $|\theta_b(t+1)-\theta_b(t)| > \delta_\theta$ or $|\theta_t(t+1)-\theta_t(t)| > \delta_\theta$ with $\delta_\theta = 5°$—we re-initialize $\mathbf{w}_{t+1}^{(0)}$ via LCMV beamforming toward the updated Bob/target directions to ensure feasibility of the power and sidelobe constraints. This warm-starting strategy significantly accelerates convergence across multi-slot passes.

E. Computational Complexity

The per-slot AO complexity is dominated by three operations: (i) SOCP projection in the $\mathbf{w}$-update (Sec. VI-B1), with complexity $\mathcal{O}(N_t^3 \cdot |\Theta_e| \cdot |\mathcal{F}|)$ due to the augmented uncertainty grid; (ii) SDP feasibility check in the $\mathbf{Q}$-update (Sec. VI-B2), with complexity $\mathcal{O}(N_t^3)$; and (iii) regularized MVDR in the $\mathbf{h}_{\rm pc}$-update, with complexity $\mathcal{O}(N^3)$ where $N = N_t L$ is the space-time dimension. The overall per-iteration complexity is:

$$\mathcal{O}\left(N_t^3 \cdot |\Theta_e| \cdot |\mathcal{F}| + N^3\right). \tag{41}$$

The per-iteration cost scales linearly with the grid sizes $|\Theta_e|$ and $|\mathcal{F}|$, and cubically with the array size N_t and space-time dimension N. For typical LEO parameters ($|\mathcal{T}| = 20$ slots, $|\mathcal{F}| = 11$ Doppler samples), the full-pass optimization is feasible for offline mission planning or slow-loop adaptation.

VIII. Numerical Results

In this section, we provide numerical results to evaluate the effectiveness of the proposed LEO-robust ISAC beamforming framework. We assume that both the ISAC transmitter and radar receiver are equipped with uniform linear arrays (ULAs) with half-wavelength spacing between adjacent antennas. The default simulation setup comprises: $N_t = N_r = 16$ element ULA, $N = 64$ fast-time samples, $L = 16$ slow-time pulses, and pulse repetition interval $T_r = 100\,\mu$s; HAPS altitude 20 km, LEO altitude 550 km, Bob at $\theta_b = -60°$, target at $\theta_t = 0°$, eavesdropper sector $\Theta_e = [32°, 38°]$; Bob and Eve path losses -80 dB and -85 dB respectively, noise powers $\sigma_b^2 = \sigma_e^2 = -100$ dBm, K-distributed sea clutter with shape parameter $\nu = 2$, self-interference $\sigma_{\rm SI}^2 = -90$ dBm, clutter Doppler spread $\sigma_f = 4$ Hz; sidelobe suppression $\gamma = -20$ dB over $\Omega_{\rm SL}$; $|\mathcal{T}| = 20$ slots of 10 s duration, Doppler grid $|\mathcal{F}| = 11$ spanning ± 5 kHz, angular grid $1°$ resolution.

We employ a Gaussian prior on the target state $\boldsymbol{\eta} = [\tau_t, \theta_t, f_D]^T$ with prior information matrix $\mathbf{J}_P = \mathrm{diag}(1/\sigma_\tau^2, 1/\sigma_\theta^2, 1/\sigma_{f_D}^2)$ and prior standard deviations $(\sigma_\tau, \sigma_\theta, \sigma_{f_D}) = (0.2\,T_s, 0.5°, 2$ Hz$)$. These values reflect realistic maritime target tracking scenarios with moderate prior uncertainty. In experiments, we compute the derivatives $(\partial \boldsymbol{\mu}/\partial \boldsymbol{\eta})$ via centered finite differences with steps δ_τ=$0.1\,T_s$, δ_θ=$0.1°$, δ_{f_D}=0.5 Hz, ensuring numerical accuracy while maintaining computational efficiency.

Resultant Pareto frontiers of the proposed LEO-robust ISAC design are shown in Fig. 2, which demonstrate the trade-off between sensing performance $\widehat{\Psi} = \Psi/\Psi_0$ and worst-case secrecy rate $\widehat{\rm SR}_{\min} = {\rm SR}_{\min}/{\rm SR}_0$. The frontier is generated by sweeping $\alpha_{\rm ws} \in [0,1]$ and is smooth and monotone, consistent with the weighted-sum formulation in Problem (P). The proposed LEO-robust design (solid curve) achieves a superior boundary compared to the LEO-agnostic baseline (dashed curve), which fails to compensate for Doppler-induced inter-carrier interference. Endpoints mark the radar-only ($\widehat{\Psi} \approx 1$) and comm-only ($\widehat{\rm SR}_{\min} \approx 1$) baselines. The gap between the two curves quantifies the benefit of the proposed ICI-aware effective noise modeling and multi-slot parameterization for LEO scenarios.

Convergence behavior of the proposed alternating optimization (AO) algorithm is illustrated in Fig. 3, which shows the evolution of worst-case secrecy rate and sensing root-BCRB across iterations for three weighting configurations: sensing-dominant ($\alpha_{\rm ws} = 0.9$), balanced ($\alpha_{\rm ws} = 0.5$), and secrecy-dominant ($\alpha_{\rm ws} = 0.1$). Both metrics converge monotonically and stabilize within about 5 iterations across all configurations, confirming the monotonic convergence property of the AO algorithm. The rapid convergence validates the practical efficiency of the solver for real-time deployment scenarios. Notably, the convergence speed is relatively insensitive to the weighting parameter $\alpha_{\rm ws}$, indicating robust algorithmic behavior across different optimization objectives.

The robustness of the LEO-robust design to Doppler frequency offset is demonstrated in Fig. 4, which compares the performance of the proposed LEO-robust design against a LEO-agnostic baseline that ignores inter-carrier interference. The LEO-agnostic baseline, optimized for zero Doppler offset, exhibits catastrophic performance collapse as the residual

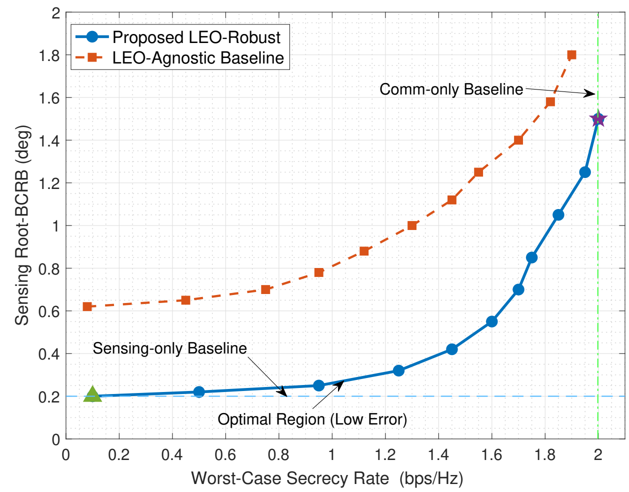

Fig. 2. Pareto frontier between sensing and secrecy performance. LEO-robust design (solid) achieves a superior boundary compared to the LEO-agnostic baseline (dashed). Frontier generated by sweeping $\alpha_{\rm ws} \in [0,1]$.

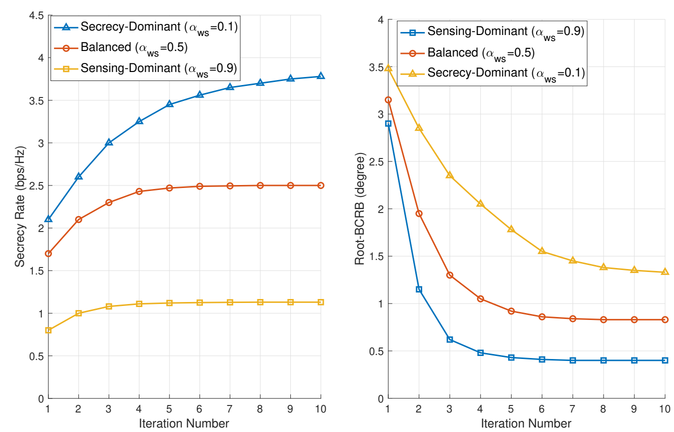

(a) SR Convergence (b) Root-BCRB Convergence

Fig. 3. Convergence of AO algorithm for three weighting configurations: $\alpha_{\rm ws} \in \{0.9, 0.5, 0.1\}$. Both worst-case SR and sensing root-BCRB stabilize within around 5 iterations.

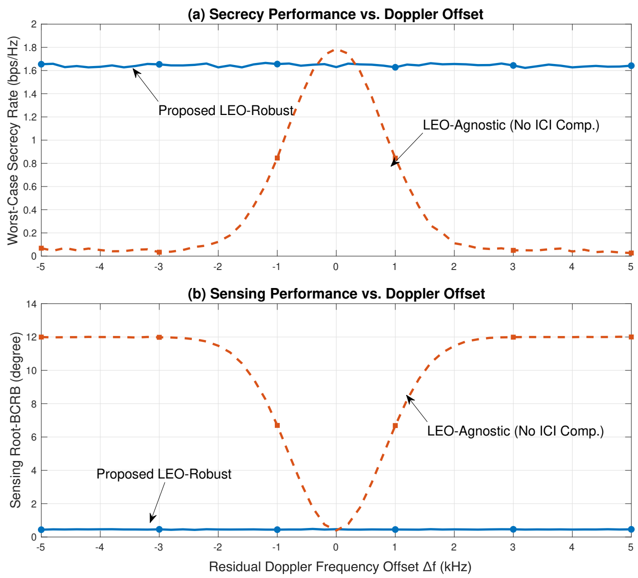

Fig. 4. Impact of residual Doppler offset Δf on (a) worst-case SR and (b) sensing root-BCRB. LEO-robust design (solid) maintains stable performance across ± 5 kHz, while LEO-agnostic baseline (dashed) degrades beyond ± 3 kHz.

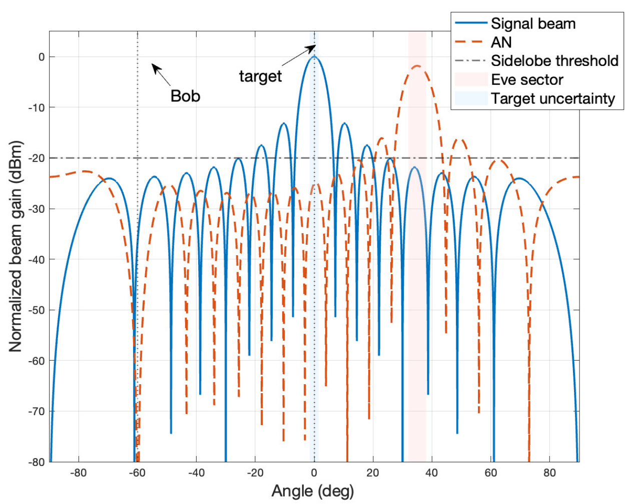

Fig. 5. Optimized transmit beampattern for $N_t = 16$, $\alpha_{\mathrm{ws}} = 0.5$. Solid: signal beam power. Dashed: artificial noise power. Signal beam spans target ($\theta_t = 0^\circ$). AN forms null at Bob and concentrates power in eavesdropper sector $\Theta_e = [32^\circ, 38^\circ]$.

Doppler frequency offset $|\Delta f|$ increases beyond ± 3 kHz, with worst-case SR dropping below the compliance threshold $R_0 = 1.5$ bps/Hz and sensing root-BCRB degrading by more than 50%. In contrast, the LEO-robust design maintains stable performance across the full ± 5 kHz Doppler range, with less than 10% performance loss relative to the zero-offset case. This dramatic difference demonstrates the necessity of the proposed ICI-aware effective noise modeling and multi-slot parameterization for reliable LEO-ISAC operation.

Optimized beampatterns for the balanced weighting configuration ($\alpha_{\mathrm{ws}} = 0.5$) with $N_t = 16$ antennas are shown in

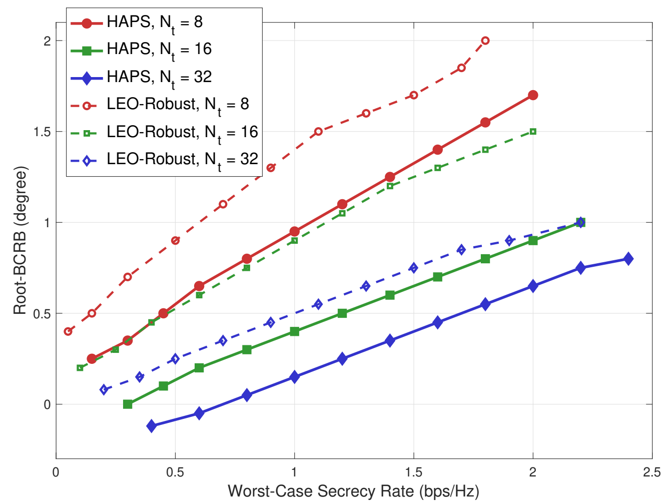

Fig. 6. Impact of transmit array size $N_t \in \{8, 16, 32\}$ on Pareto frontier. Solid: HAPS-only. Dashed: LEO-robust design. Increasing N_t improves the sensing-secrecy trade-off for both platforms.

Fig. 5. The signal beam exhibits a flat-top mainlobe with approximately 6.3° 3-dB beamwidth centered at the target direction ($\theta_t = 0^\circ$), with sidelobes suppressed to -20 dB across the sidelobe region Ω_{SL}. The beamformer simultaneously maintains a deep null at the legitimate user's location ($\theta_b = -60^\circ$) to prevent unintended signal leakage. The AN pattern forms a deep null at Bob's location (enforcing the Bob-null constraint $\mathbf{h}_b^H \mathbf{Q} \mathbf{h}_b = 0$) and concentrates power in the eavesdropper sector $\Theta_e = [32^\circ, 38^\circ]$, where the AN power significantly exceeds the signal power. This spatial structure exemplifies the joint optimization of sensing and security objectives: the signal beamformer maximizes target illumination while the AN covariance degrades eavesdropper reception without affecting the legitimate user Bob.

The impact of transmit array size on the Pareto frontier is shown in Fig. 6, where we sweep $N_t \in \{8, 16, 32\}$ for both HAPS-only (ideal platform without Doppler/ICI) and LEO-robust designs. Increasing N_t shifts the frontier toward the desirable lower-right region, corresponding to lower sensing root-BCRB and higher worst-case secrecy rate. This demonstrates that additional spatial degrees of freedom improve the sensing–secrecy trade-off. For each array size, the HAPS-only design generally attains a more favorable frontier than the LEO-robust design, while the latter reflects the performance cost of Doppler/ICI robustness.

Robustness to eavesdropper angular uncertainty is evaluated in Fig. 7, where we vary the eavesdropper sector width $|\Theta_e| \in [1^\circ, 10^\circ]$ for array sizes $N_t \in \{8, 16, 32\}$. As $|\Theta_e|$ increases, both worst-case SR and sensing root-BCRB degrade gracefully: SR decreases because wider uncertainty requires more AN power to maintain secrecy, and sensing error increases because fewer spatial degrees of freedom are available for target illumination. At $|\Theta_e| = 10^\circ$, the HAPS platform with $N_t = 32$ achieves $\mathrm{SR}_{\min} \approx 1.79$ bps/Hz and root-BCRB $\approx 0.21^\circ$, while the LEO-robust design achieves approximately 1.64 bps/Hz and 0.31°, respectively. The HAPS-only design

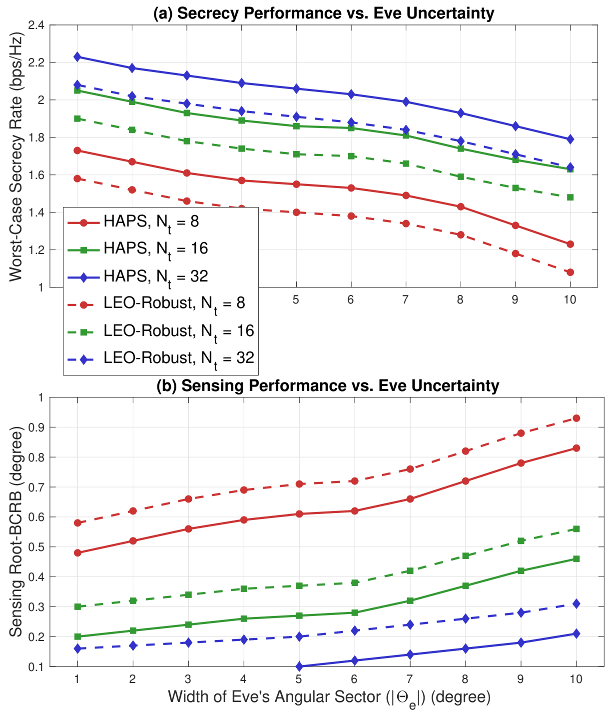

Fig. 7. Impact of eavesdropper angular uncertainty $|\Theta_e| \in [1^\circ, 10^\circ]$ on (a) worst-case SR and (b) sensing root-BCRB, for $N_t \in \{8, 16, 32\}$. Solid: HAPS-only. Dashed: LEO-robust. Both metrics degrade gracefully as $|\Theta_e|$ increases.

maintains a consistent performance advantage over the LEO-robust design, reflecting the cost of Doppler/ICI robustness.

Sensitivity to pulse compression imperfections is examined in Fig. 8, where we introduce fractional delay interpolation errors with normalized variance $\sigma^2_{\tau,\text{interp}}/T_s^2 \in [0, 0.1]$ for array sizes $N_t \in \{8, 16, 32\}$. For all configurations, the sensing root-BCRB increases gracefully with interpolation error, demonstrating sensitivity to this practical signal-processing imperfection. At $\sigma^2_{\tau,\text{interp}}/T_s^2 = 0.1$, the root-BCRB increases from approximately 0.08° to 0.16° for $N_t = 32$ and from 0.40° to 0.80° for $N_t = 8$. Larger arrays retain lower absolute sensing error throughout the interpolation-error range. This validates the effective-noise model developed in Section III-C.

IX. Conclusion

This paper presented a secure ISAC beamforming framework for maritime networks integrating HAPS and LEO platforms. By jointly optimizing the transmit beamformer, Bob-null artificial noise covariance, and pulse compression filter, the proposed AO algorithm achieves tunable trade-offs between sensing accuracy under SIRP sea clutter and worst-case SR over eavesdropper angular sectors. The BFIM with log-det criterion provides rigorous multi-parameter estimation bounds, while maintaining computational tractability. For LEO scenarios, per-slot parameterization absorbs Doppler-induced inter-carrier interference into effective noise terms, enabling warm-started optimization across orbital passes without modifying the core algorithm. Simulations demonstrate smooth Pareto frontiers, robustness to sea state variations, and stable

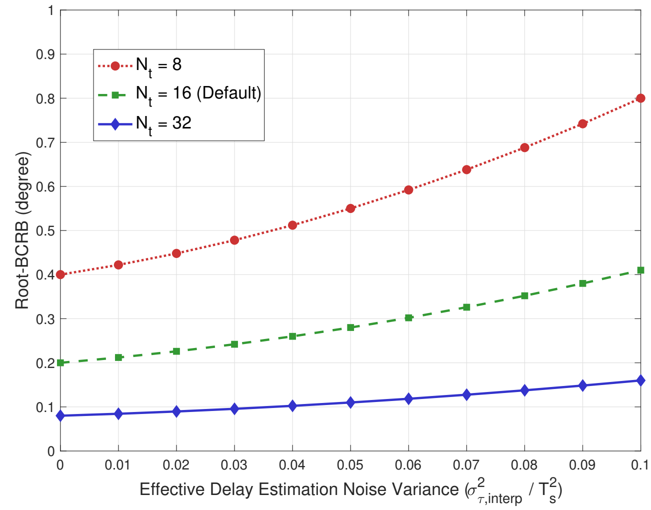

Fig. 8. Impact of fractional delay interpolation error on sensing root-BCRB for $N_t \in \{8, 16, 32\}$. X-axis: normalized interpolation noise variance $\sigma^2_{\tau,\text{interp}}/T_s^2 \in [0, 0.1]$. Sensing error increases gracefully with interpolation error.

convergence across LEO time slots. The framework is limited to LoS maritime scenarios with angularly separable users; near-collinear geometries require alternative security mechanisms. Future work includes multi-user extensions, wideband waveform co-design, and joint scheduling for hybrid HAPS-LEO constellations.

Appendix A
Proof of Lemma 1

Proof (Conservativeness of ICI-as-Noise Approximation): This appendix provides the complete proof of Lemma 1, which establishes that treating ICI as additive Gaussian noise yields a conservative lower bound on the achievable secrecy rate.

Proof: Consider the received signal at Eve's receiver in the presence of ICI:

$$\begin{aligned} y_e = &\mathbf{h}_e^H \mathbf{w} s + \mathbf{h}_e^H \mathbf{Q}^{1/2} \mathbf{z}_{\text{AN}} \\ &+ \underbrace{\sum_{k \neq 0} \sqrt{\kappa[k;\varepsilon]} \cdot \mathbf{h}_e^H (\mathbf{w} s_k + \mathbf{Q}^{1/2} \mathbf{z}_{\text{AN},k})}_{\text{ICI term}} + n_e, \end{aligned} \tag{42}$$

where s is the desired symbol, s_k are symbols from adjacent subcarriers, $\mathbf{z}_{\text{AN}}$ and $\mathbf{z}_{\text{AN},k}$ are independent AN vectors, and n_e is thermal noise.

The true mutual information is:

$$\begin{aligned} I(s; y_e | \text{ICI structure}) = &h(y_e | \text{ICI structure}) \\ &- h(y_e | s, \text{ICI structure}), \end{aligned} \tag{43}$$

where the conditioning on "ICI structure" indicates knowledge of the ICI correlation across subcarriers. By the worst-case noise lemma [49], replacing the structured ICI term with worst-case additive Gaussian noise of equal power yields a lower bound on mutual information:

$$I(s; y_e | \text{ICI structure}) \geq I(s; y_e | \text{ICI power}), \tag{44}$$

where the right-hand side corresponds to the ICI-as-noise approximation in (38).

Formally, we construct the effective noise covariance upper bound:

$$\begin{aligned}\mathbf{R}_{\text{eff}} &= \sigma_0^2\mathbf{I} + \sigma_{\text{SI}}^2\mathbf{I} \\ &+ \sum_{k\neq 0} \kappa[k;\varepsilon]\cdot(\mathbf{w}\mathbf{w}^H + \mathbf{Q}) \succeq \mathbb{E}[\text{ICI}\cdot\text{ICI}^H],\end{aligned} \tag{45}$$

where the inequality holds because we discard the correlation structure of ICI across subcarriers. This yields:

$$\begin{aligned}\text{SR}_{\text{ICI-noise}} &= \log(1+\text{SINR}_b) \\ &- \log(1+\text{SINR}_{e,\text{eff}}) \le \text{SR}_{\text{true}},\end{aligned} \tag{46}$$

where $\text{SINR}_{e,\text{eff}}$ uses the effective noise power from (38), and the inequality follows from the fact that the true SINR at Eve can only be higher when ICI structure is exploited. □

Appendix B
Proof of Proposition 1

Proof (Doppler Grid Discretization Error):

This appendix provides the complete proof of Proposition 1, which establishes the Lipschitz continuity of the secrecy rate with respect to normalized CFO ε.

Proof: We establish the Lipschitz continuity via a chain of Lipschitz functions:

Step 1: ICI Kernel Lipschitz Continuity. The ICI kernel $\kappa[k;\varepsilon] = |\text{sinc}(\varepsilon - k)|^2$ from (37) is Lipschitz continuous in ε. Taking the derivative:

$$\frac{\partial \kappa[k;\varepsilon]}{\partial \varepsilon} = 2\text{sinc}(\varepsilon - k)\cdot\frac{\partial \text{sinc}(\varepsilon - k)}{\partial \varepsilon}, \tag{47}$$

where

$$\frac{\partial \text{sinc}(x)}{\partial x} = \frac{\cos(\pi x)}{x} - \frac{\sin(\pi x)}{\pi x^2} \tag{48}$$

is bounded for $|x| \ge 1$. For the truncated summation $|k| \le K_{\max}$, we have:

$$\left|\frac{\partial \kappa[k;\varepsilon]}{\partial \varepsilon}\right| \le C_\kappa, \quad \text{for all } |k| \le K_{\max}, \tag{49}$$

where $C_\kappa = \mathcal{O}(1)$ is a constant independent of ε.

Step 2: Effective Noise Lipschitz Continuity. The effective noise power $\sigma_{e,\text{eff}}^2(\theta,\varepsilon)$ from (38) is:

$$\sigma_{e,\text{eff}}^2(\theta,\varepsilon) = \sigma_0^2 + \sigma_{\text{SI}}^2 + \sum_{k\neq 0}\kappa[k;\varepsilon]\cdot P_{\text{TX}}\cdot|\mathbf{h}_e(\theta)|^2. \tag{50}$$

For fixed θ, the channel gain $|\mathbf{h}_e(\theta)|^2$ is constant, so taking the derivative with respect to ε:

$$\begin{aligned}\left|\frac{\partial \sigma_{e,\text{eff}}^2(\theta,\varepsilon)}{\partial \varepsilon}\right| &= \left|\sum_{k\neq 0}\frac{\partial \kappa[k;\varepsilon]}{\partial \varepsilon}\cdot P_{\text{TX}}\cdot|\mathbf{h}_e(\theta)|^2\right| \\ &\le 2K_{\max}\cdot C_\kappa\cdot P_{\text{TX}}\cdot|\mathbf{h}_e(\theta)|^2 \triangleq L_\sigma(\theta).\end{aligned} \tag{51}$$

Step 3: Secrecy Rate Lipschitz Continuity. The secrecy rate is:

$$\begin{aligned}\text{SR}(\varepsilon) &= \log\left(1 + \frac{|\mathbf{h}_b^H\mathbf{w}|^2}{\sigma_{b,\text{eff}}^2(\varepsilon)}\right) \\ &- \log\left(1 + \frac{|\mathbf{h}_e^H\mathbf{w}|^2}{\mathbf{h}_e^H\mathbf{Q}\mathbf{h}_e + \sigma_{e,\text{eff}}^2(\varepsilon)}\right).\end{aligned} \tag{52}$$

Taking the derivative with respect to ε, let $S_b \triangleq |\mathbf{h}_b^H\mathbf{w}|^2$, $S_e \triangleq |\mathbf{h}_e^H\mathbf{w}|^2$, $A_e \triangleq \mathbf{h}_e^H\mathbf{Q}\mathbf{h}_e$, and $\sigma_b \triangleq \sigma_{b,\text{eff}}^2(\varepsilon)$, $\sigma_e \triangleq \sigma_{e,\text{eff}}^2(\varepsilon)$:

$$\frac{\partial \text{SR}}{\partial \varepsilon} = -\frac{S_b}{(\sigma_b + S_b)\sigma_b}\cdot\frac{\partial \sigma_b}{\partial \varepsilon} - \frac{S_e}{(A_e + \sigma_e + S_e)(A_e + \sigma_e)}\cdot\frac{\partial \sigma_e}{\partial \varepsilon}. \tag{53}$$

Bounding the derivative:

$$\begin{aligned}\left|\frac{\partial \text{SR}(\varepsilon)}{\partial \varepsilon}\right| &\le \frac{L_\sigma}{\sigma_{\min}^2}\cdot\left(\frac{|\mathbf{h}_b^H\mathbf{w}|^2}{\sigma_{b,\text{eff}}^2(\varepsilon)} + \frac{|\mathbf{h}_e^H\mathbf{w}|^2}{\mathbf{h}_e^H\mathbf{Q}\mathbf{h}_e + \sigma_{e,\text{eff}}^2(\varepsilon)}\right) \\ &\le \frac{L_\sigma}{\sigma_{\min}^2}\cdot(1 + \text{SINR}_{\max}) \triangleq L_{\text{SR}},\end{aligned} \tag{54}$$

where $\sigma_{\min}^2 = \min(\sigma_0^2, \sigma_{\text{SI}}^2)$ and $\text{SINR}_{\max}$ is the maximum SINR across all scenarios (accounting for both signal and AN contributions).

By the mean-value theorem, for any $\varepsilon, \hat{\varepsilon} \in [-1,+1]$:

$$|\text{SR}(\varepsilon) - \text{SR}(\hat{\varepsilon})| \le L_{\text{SR}}\cdot|\varepsilon - \hat{\varepsilon}|. \tag{55}$$

□

Remark: For typical system parameters ($P_0 = 1$, $\sigma_0^2 = -100$ dBm, $K_{\max} = 10$), the Lipschitz constant is $L_{\text{SR}} \approx 5$–10 bps/Hz per unit normalized CFO. For the default grid spacing $\delta_{\mathcal{F}} = 0.067$ (1 kHz), the discretization error is bounded by $L_{\text{SR}}\cdot\delta_{\mathcal{F}} \approx 0.3$–0.7 bps/Hz, which is small compared to typical secrecy rates (1–3 bps/Hz).

References

[1] F. Liu, Y. Cui, C. Masouros, J. Xu, T. X. Han, Y. C. Eldar, and S. Buzzi, "Integrated sensing and communications: Toward dual-functional wireless networks for 6G and beyond," *IEEE J. Sel. Areas Commun.*, vol. 40, no. 6, pp. 1728–1767, Jun. 2022.

[2] Z. Li and B. Shang, "Fundamentals of satellite-maritime communications: Downlink and uplink analysis," *IEEE Trans. Commun.*, vol. 73, no. 4, pp. 2191–2206, Apr. 2025.

[3] A. Mukherjee, S. A. A. Fakoorian, J. Huang, and A. L. Swindlehurst, "Principles of physical layer security in multiuser wireless networks: A survey," *IEEE Commun. Surveys Tuts.*, vol. 16, no. 3, pp. 1550–1573, 2014, third Quarter.

[4] L. Rosenberg, S. Watts, and M. S. Greco, "Modeling the statistics of microwave radar sea clutter," *IEEE Aerosp. Electron. Syst. Mag.*, vol. 34, no. 10, pp. 44–75, Oct. 2019.

[5] E. Conte, M. Lops, and G. Ricci, "Asymptotically optimum radar detection in compound-gaussian clutter," *IEEE Trans. Aerosp. Electron. Syst.*, vol. 31, no. 2, pp. 617–625, Apr. 1995.

[6] H. He, Z. Li, X. Zhang, J. Jia, Y. He, and Y. You, "Characteristic description and statistical model-based method for sea clutter modeling," *Remote Sens.*, vol. 16, no. 23, p. 4429, 2024.

[7] X. Chen, K. Liu, Z. Zhang, and H. Deng, "Mixture texture model with weighted generalized inverse gaussian distribution for target detection," *Digit. Signal Process.*, vol. 154, p. 104677, 2024.

[8] Y.-C. Zhang and P.-L. Shui, "Robust speckle covariance matrix estimation of sea clutter based on spectral symmetry," *Signal Process.*, vol. 224, p. 109590, 2024.

[9] A. A. Salem, S. Abdallah, M. Saad, K. Alnajjar, and M. A. Albreem, "Robust secure ISAC: How RSMA and active RIS manage eavesdropper's spatial uncertainty," *IEEE Trans. Veh. Technol.*, vol. 75, no. 3, pp. 4383–4398, Mar. 2026.

[10] J. Bai, H.-M. Wang, and P. Liu, "Robust IRS-aided secrecy transmission with location optimization," *IEEE Trans. Commun.*, vol. 70, no. 9, pp. 6149–6163, Sep. 2022.

[11] X. Lin *et al.*, "Doppler shift estimation in 5G new radio non-terrestrial networks," in *Proc. IEEE Glob. Commun. Conf.* IEEE, 2021, pp. 1–6.

[12] A. K. Meshram, S. Kumar, J. Querol, and S. Chatzinotas, "Beam centric doppler pre-compensation for LEO-based 5G-NTN," in *Proc. IET Conf.* IET, 2023, pp. 23–28.

[13] Y. Zhang, Y. Gang, P. Wu, G. Fan, W. Xu, B. Ai, and Q. Wu, "Integrated sensing, communication, and computation in SAGIN: Joint beamforming and resource allocation," *IEEE Trans. Cogn. Commun. Netw.*, vol. 11, no. 5, pp. 3128–3143, Oct. 2025.

[14] S. Li, F. Zhang, T. Mao, R. Na, Z. Wang, and G. K. Karagiannidis, "Transmit beamforming design for ISAC with stacked intelligent metasurfaces," *IEEE Trans. Veh. Technol.*, vol. 74, no. 4, pp. 6767–6772, Apr. 2025.

[15] T. Mao, L. Zhang, Z. Xiao, Z. Han, and X.-G. Xia, "Terahertz-band near-space communications: From a physical-layer perspective," *IEEE Commun. Mag.*, vol. 62, no. 2, pp. 110–116, Feb. 2024.

[16] S. Fodor, G. Fodor, and M. Telekz, "On the trade-off between angle of arrival and symbol estimation in bistatic ISAC systems using unitary signaling," *IEEE Trans. Commun.*, vol. 73, no. 7, pp. 5328–5343, Jul. 2025.

[17] M. Zhu, L. Li, S. Xia, and T.-H. Chang, "Information and sensing beamforming optimization for multi-user multi-target MIMO ISAC systems," *EURASIP J. Adv. Signal Process.*, vol. 2023, no. 1, p. 15, 2023.

[18] X. Liu, T. Huang, N. Shlezinger, Y. Liu, J. Zhou, and Y. C. Eldar, "Joint transmit beamforming for multiuser MIMO communications and MIMO radar," *IEEE Trans. Signal Process.*, vol. 68, pp. 3929–3944, 2020.

[19] K. M. Attiah and W. Yu, "Beamforming design for integrated sensing and communications using uplink-downlink duality," in *Proc. IEEE Int. Symp. Inf. Theory*. IEEE, 2024, pp. 2808–2813.

[20] Y. Wang, M. Tao, and S. Sun, "Cramér-Rao bound analysis and beamforming design for integrated sensing and communication with extended targets," *IEEE Trans. Wireless Commun.*, vol. 23, no. 11, pp. 15 987–16 000, Nov. 2024.

[21] J. Zhang, W. Lu, C. Xing, N. Zhao, N. Al-Dhahir, G. K. Karagiannidis, and X. Yang, "Intelligent integrated sensing and communication: A survey," *Sci. China Inf. Sci.*, vol. 68, no. 3, p. 131301, 2025.

[22] P. Stoica and A. Nehorai, "MUSIC, maximum likelihood, and Cramér-Rao bound," *IEEE Trans. Acoustics, Speech, Signal Process.*, vol. 37, no. 5, pp. 720–741, May 1989.

[23] N. Su, F. Liu, and C. Masouros, "Sensing-assisted eavesdropper estimation: An ISAC breakthrough in physical layer security," *IEEE Trans. Wireless Commun.*, vol. 23, no. 4, pp. 3162–3174, Apr. 2024.

[24] O. Besson and Y. I. Abramovich, "On the fisher information matrix for multivariate elliptically contoured distributions," *IEEE Signal Process. Lett.*, vol. 20, no. 11, pp. 1130–1133, Nov. 2013.

[25] E. M. Abadi, C. Goken, C. Ozturk, and S. Gezici, "Optimal power allocation and optimal linear encoding for parameter estimation in the presence of a smart eavesdropper," *IEEE Trans. Signal Process.*, vol. 70, pp. 4093–4108, 2022.

[26] E. M. Abadi, A. N. Hokmabadi, and S. Gezici, "Joint RIS phase profile design and power allocation for parameter estimation in presence of eavesdropping," *IEEE Trans. Veh. Technol.*, vol. 73, no. 12, pp. 19 186–19 202, Dec. 2024.

[27] X. Li, V. C. Andrei, U. J. Mönich, and H. Boche, "Optimal and robust waveform design for MIMO-OFDM channel sensing: A Cramér-Rao bound perspective," in *Proc. IEEE Int. Conf. Commun.* IEEE, 2023, pp. 3516–3521.

[28] R. Kaur, B. Bansal, S. Majhi, S. Jain, C. Huang, and C. Yuen, "A survey on reconfigurable intelligent surface for physical layer security of next-generation wireless communications," *IEEE Open J. Veh. Technol.*, vol. 5, pp. 172–199, 2024.

[29] H. Son, "Performance analysis of artificial-noise-based secure transmission in wiretap channel," *Mathematics*, vol. 13, no. 1, p. 32, 2024.

[30] N. Su, F. Liu, and C. Masouros, "Secure radar-communication systems with malicious targets: Integrating radar, communications and jamming functionalities," *IEEE Trans. Wireless Commun.*, vol. 20, no. 1, pp. 83–95, Jan. 2021.

[31] Z. Chen, S. Zhu, X. Li, and Y. Liu, "Secure transmission of integrated sensing and communication systems with eavesdropper: From mainlode to sidelode deployment," *IEEE Trans. Veh. Technol.*, vol. 74, no. 9, pp. 13 894–13 908, Sep. 2025.

[32] F. S. Alqurashi, A. Trichili, N. Saeed, B. S. Ooi, and M.-S. Alouini, "Maritime communications: A survey on enabling technologies, opportunities, and challenges," *IEEE Internet Things J.*, vol. 10, no. 4, pp. 3525–3547, Feb. 2023.

[33] Y. Wang, W. Feng, J. Wang, and T. Q. S. Quek, "Hybrid satellite-UAV-terrestrial networks for 6G ubiquitous coverage: A maritime communications perspective," *IEEE J. Sel. Areas Commun.*, vol. 39, no. 11, pp. 3475–3490, Nov. 2021.

[34] S. Plastras, D. Tsoumatidis, D. N. Skoutas, A. Rouskas, G. Kormentzas, and C. Skianis, "Non-terrestrial networks for energy-efficient connectivity of remote IoT devices in the 6G era: A survey," *Sensors*, vol. 24, no. 4, p. 1227, 2024.

[35] Y. Zhao and S.-G. Haggman, "Intercarrier interference self-cancellation scheme for OFDM mobile communication systems," *IEEE Trans. Commun.*, vol. 49, no. 7, pp. 1185–1191, Jul. 2001.

[36] O. Nia and B. L. Mark, "Models for frequency doppler shift prediction for LEO satellites at L-band," in *Proc. IEEE Mil. Commun. Conf.* IEEE, 2022, pp. 623–628.

[37] Y. Liu, M. Chen, C. Pan, T. Gong, J. Yuan, and J. Wang, "OTFS vs OFDM: Which is superior in multiuser LEO satellite communications," *IEEE J. Sel. Areas Commun.*, vol. 43, no. 1, pp. 139–155, Jan. 2025.

[38] M.-G. Kim and H.-S. Jo, "Performance analysis of NB-IoT uplink in low earth orbit non-terrestrial networks," *Sensors*, vol. 22, no. 18, p. 7097, 2022.

[39] Q. Chen, Z. Wang, G. F. Pedersen, and M. Shen, "Joint satellite-transmitter and ground-receiver digital pre-distortion for active phased arrays in LEO satellite communications," *Remote Sens.*, vol. 14, no. 17, p. 4319, 2022.

[40] Y.-C. Pai and J.-F. Kiang, "Statistical parameters extracted from radar sea clutter simulated under different operational conditions," *Sensors*, vol. 24, no. 12, p. 3720, 2024.

[41] A. H. M. Mboungam, Y. Zhi, and C. K. F. Monguen, "Constant false alarm rate detection method in mixed weibull distribution sea clutter," *Digit. Signal Process.*, vol. 149, p. 104494, 2024.

[42] M. Trinh-Hoang, M. Viberg, and M. Pesavento, "Cramér-Rao bound for DOA estimators under the partial relaxation framework: Derivation and comparison," *IEEE Trans. Signal Process.*, vol. 68, pp. 3194–3208, 2020.

[43] B. Huang, S. Ahmed, and M.-S. Alouini, "Design of frequency index modulated waveforms for integrated SAR and communication on high-altitude platforms (HAPs)," *IEEE Trans. Commun.*, vol. 73, no. 11, pp. 12 869–12 883, Nov. 2025.

[44] A. Aubry, V. Carotenuto, A. De Maio, and F. Fioranelli, "Compatibility assessment of multistatic/polarimetric clutter data with the SIRP model," *IEEE Trans. Aerosp. Electron. Syst.*, vol. 59, no. 1, pp. 359–374, Feb. 2023.

[45] J. Ward, "Space-time adaptive processing for airborne radar," in *Proc. IEE Colloq. Space-Time Adaptive Process.* IEE, 1998, pp. 2/1–2/6.

[46] E. Chaumette, B. Priot, F. Vincent, G. Pages, and A. Dion, "Minimum variance distortionless response estimators for linear discrete state-space models," *IEEE Trans. Autom. Control*, vol. 62, no. 4, pp. 2048–2055, Apr. 2017.

[47] P. H. Moose, "A technique for orthogonal frequency division multiplexing frequency offset correction," *IEEE Trans. Commun.*, vol. 42, no. 10, pp. 2908–2914, Oct. 1994.

[48] U. Mengali, *Synchronization Techniques for Digital Receivers*. Berlin, Germany: Springer Science & Business Media, 2013.

[49] A. Goldsmith, *Wireless Communications*. Cambridge, U.K.: Cambridge Univ. Press, 2005.

Nanchi Su (Member, IEEE) received the B.E. and M.E. degrees from the Harbin Institute of Technology, Heilongjiang, China, in 2015 and 2018, respectively, and the Ph.D. degree from University College London, London, U.K., in 2023. She is currently an Associate Professor with the Guangdong Provincial Key Laboratory of Aerospace Communication and Networking Technology, Harbin Institute of Technology (Shenzhen), Shenzhen, China. Her research interests include integrated sensing and communication systems (ISAC), multi-agent communication systems, SAGIN, and situational awareness. She serves as the Lead Guest Editor of a Special Issue of the IEEE OJ-COMS and serves as workshop Co-Chair for IEEE ICC, WCNC, PIMRC, and Globecom, etc.

Zhongxiang Wei (Senior Member, IEEE) received the Ph.D. degree in electrical and electronics engineering from the University of Liverpool, Liverpool, U.K., in 2017. From March 2016 to March 2017, he was a Research Assistant with the Institution for Infocomm Research, A*STAR, Singapore. From March 2018 to March 2021, he was a Research Associate with the Department of Electrical and Electronics Engineering, University College London. He is currently an Associate Professor with the College of Electronic and Information Engineering, Tongji University, China. He has authored or co-authored more than 100 research papers published on top-tier journals and international conferences. His research interests include trustworthy 6G, MIMO communications, and algorithm design. He has acted as the Session/Track Chair of various international conferences, such as IEEE ICC/GLOBECOM/ICASSP/VTC and has acted as a Guest Editor of IEEE Internet of Things Journal, IEEE Open Journal on Vehicular Technology, and IEEE Journal of Selected Topics in Signal Processing. He was a recipient of Shanghai Leading Talent Program (Young Scientist) in 2021, the Best Paper Award of IEEE IWCMC in 2024, Stanford World Top 2% Scientist in 2025, the Outstanding Self Financed Students Abroad in 2018, and the A*STAR Research Attachment Program (ARAP) in 2016.

Xiaoye Jing (Member, IEEE) is an Associate Professor with the School of Electrical Engineering & Intelligentization, Dongguan University of Technology, China. Her research interests include integrated sensing and communication (ISAC), low-altitude communications, and space-air-ground integrated networks. She has served as a TPC member for IEEE flagship conferences.

Yao Shi (Member, IEEE) received her Ph.D. degree in Electrical and Electronic Engineering from the University of Manchester, UK. She joined Harbin Institute of Technology (Shenzhen) in 2021 and currently serves as an Associate Professor in the School of Information Science and Technology. Her research interests include integrated satellite-terrestrial networks, UAV communications, B5G/6G uplink enhancement technologies, and multimodal data fusion.

Weijie Yuan (Senior Member, IEEE) is a tenured Associate Professor with the Southern University of Science and Technology, Shenzhen, China. He serves as an Associate Editor for the *IEEE Transactions on Communications*, the *IEEE Transactions on Wireless Communications*, and the *IEEE Transactions on Mobile Computing*. He has also served as a Lead Guest Editor for the *IEEE Transactions on Vehicular Technology* and the *IEEE Journal of Selected Topics in Signal Processing*. He is the Founding Chair of the IEEE AESS Technical Working Group on Low-Altitude Wireless Networks.

Qinyu Zhang (Senior Member, IEEE) received the Ph.D. degree in biomedical and electrical engineering from the University of Tokushima, Tokushima, Japan, in 2003. From 1999 to 2003, he was an Assistant Professor with the University of Tokushima. He has been with the Harbin Institute of Technology (Shenzhen) since 2003, and is currently a Full Professor and Dean of the EIE School in HITsz. He is the Director of the Guangdong Provincial Key Laboratory of Aerospace Communication and Networking Technology, Shenzhen. His research interests include aerospace communications and networks, wireless communications.

Tse-Tin Chan (Member, IEEE) received the B.Eng. and Ph.D. degrees in information engineering from The Chinese University of Hong Kong (CUHK), Hong Kong, China, in 2014 and 2020, respectively. From 2020 to 2022, he was an Assistant Professor with the Department of Computer Science, The Hang Seng University of Hong Kong (HSUHK), Hong Kong. He is currently an Assistant Professor with the Department of Mathematics and Information Technology, The Education University of Hong Kong (EdUHK), Hong Kong. His research interests include wireless communications and networking, age of information (AoI), AI-native wireless systems, and integrated sensing and communication (ISAC). He has served as a Guest Editor for the IEEE Journal of Selected Topics in Signal Processing and the IEEE Open Journal of the Communications Society. He has also served on the organizing committees and technical program committees of various flagship conferences and workshops, including IEEE ICC and IEEE GLOBECOM.